5 RESULTS AND DISCUSSION

5.1 Romi D800 Hybrid

5.1.1 Machine kinematics

Figure 26 presents the maximum real feed speed the machine was capable, as a function of the linear increments.

Figure 26 – Maximum real feed the machine is capable during the linear toolpath of 200 mm in with different programmed linear increments in $G0$.

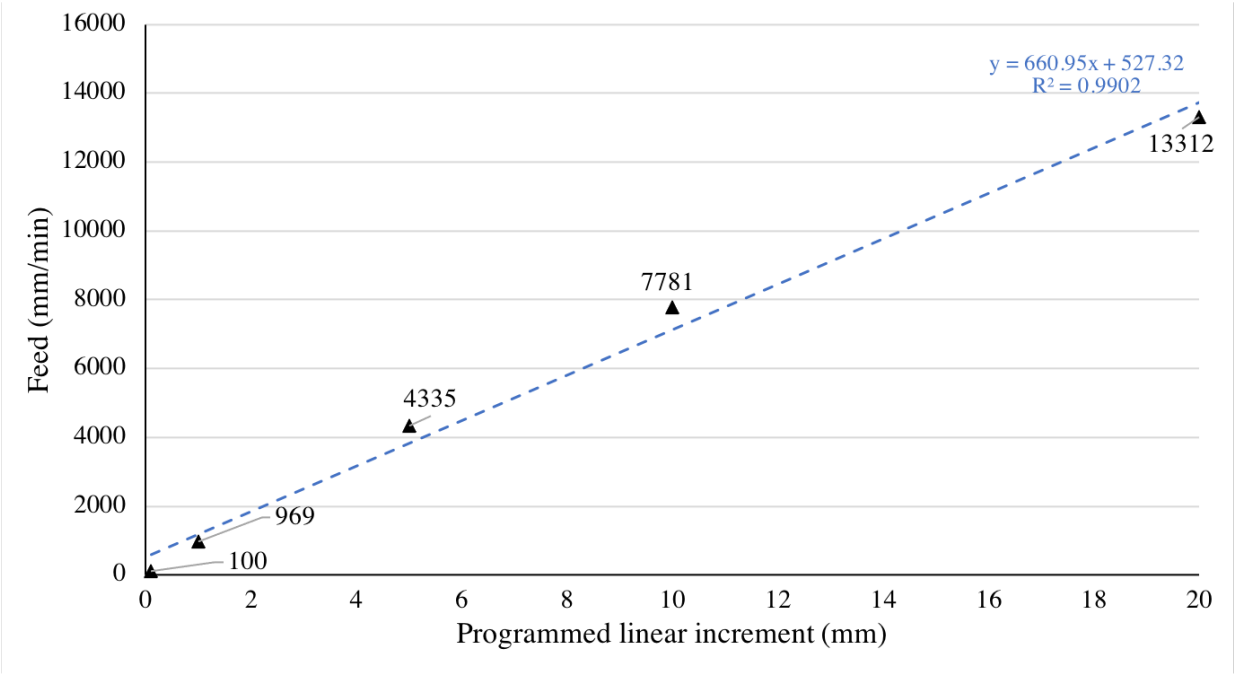

Source: Author

Although the programmed feed speed was $20,000$ mm/min (using $G0$), the data shown in Fig. 26 reveals that the real feed speed developed by the machine was always lower and varies according with the segment length. Such correlation is found to be proportionally linear ($R^2 = 0.9902$) to the length of the linear segment programmed in the g-code. This behaviour is attributed to the inertia of the moving components and to the time necessary to close the positioning loop (COELHO *et al.*, 2010). Based on this simple test, the machine can develop real feed rate higher than 600 mm/min for programmed segments higher than 0.110 mm.

The CNC data acquired during the test for verifying the machine kinematic limits is plot in Fig. 27. The graph shows the average data acquisition rate for each test performed

in G0 with different programmed linear increment. Overall, for this implementation version of DTConnect, the average DAQ was 10.03 $\pm$ 0.3 *pps*.

Figure 27 – Average data acquisition rate by DTConnect during the kinematics test at *G*0

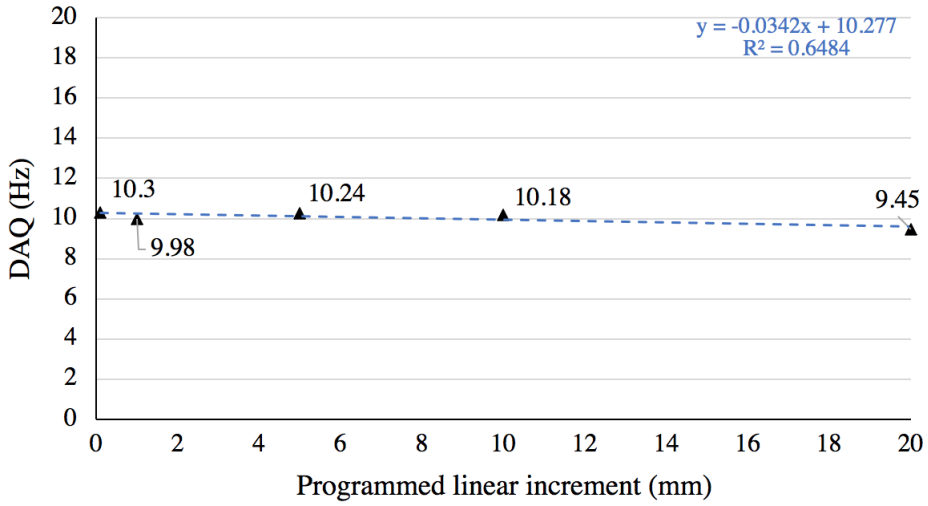

Source: Author

The same analysis were carried to the 2D and 3D geometry tests and the average DTConnect DAQ for the tests were 9.0 Hz $\pm$ 0.6 Hz and 10 Hz $\pm$ 0.2 Hz, respectively. The latest DAQ acquisition rate achieved after the last code optimization (implemented to the 3D DED tests) was found to be the higher feasible out of the hardware available. It is imperative to stress that the data sending rate from the CNC is limited due to the amount of processing occurring in parallel to the FOCAS calls to access the variables.

It has been reported that a way to increase the DAQ for this system would require an upgrade to the CNC so that the data could be transferred via optical fiber, as in the FANUC HSSB interface boards. This upgrade is costly, however the events and data calls would still be performed at random times, which would not aid much to the non-deterministic sending of data. Therefore, regarding that the melt pool images can be acquired at the range of 30 *to* 60 fps, linear regression was applied to the data from the DTConnect in order to fill in points within the data so the amount of points collected would respect the rate of 30 *pps*.

5.1.2 Powder delivery system

Figure 28 shows the plot of mass flow rate (g/min) against the rotation of the powder carrying disk, Rot H1(%).

The data with a linear and a third degree polynomial fitting are plotted in Fig. 28. The fitting curves reveals the tendency for the mass flow rate increase towards the increase

Figure 28 – Powder feeder range of mass delivery to the system

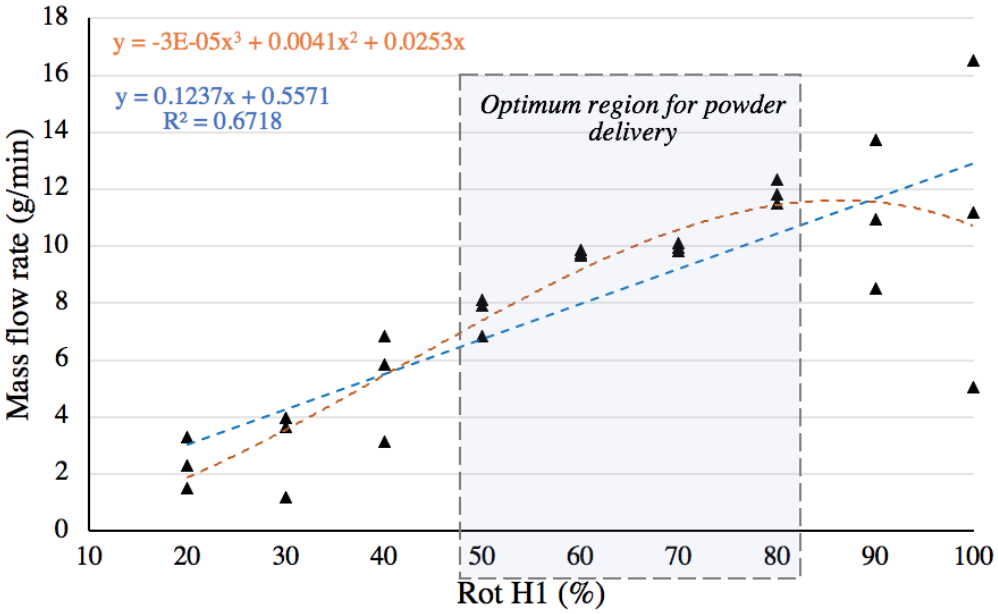

Source: Author

in the hopper disk rotation. Also, it is observed that for very low and high rotations, a higher dispersion is produced to the mass flow rate.

The reliability of systems for handling solids and small particulates of metals, in a great majority, is affected by several factors, such as the environment condition (temperature, humidity), kinematic mechanism for conveying, the conveying line from the hopper to the nozzle, etc. As one can see in Fig. 28, there is an optimum range of powder delivery, in which the system dispersion is reduced. Such operational range is delimited by the intersection of both curve fittings, and foresees mass flow rates from 6 g/min to 12 g/min, varying with the rotational speed of the disk in a near linear way.

5.1.3 Melt pool monitoring and camera setup

Figure 29 presents the track marks left on the substrate after running the laser on the substrate without powder income.

What is seen in Fig. 20 has bases on the laser polishing principle, in which the original feeding marks, left by the former milling operation, are smoothed down after local fusion/solidification provoked by the movement of the laser beam. Three regions are highlighted, representing the start/end point (O), a regular area within the linear trajectory (B) and a point of change in direction (C).

The measured values for the bead width and length were 1532.84 μm and 1577.15 μm,

Figure 29 – Melt pool track on the SS 304 substrate for pixel size calibration

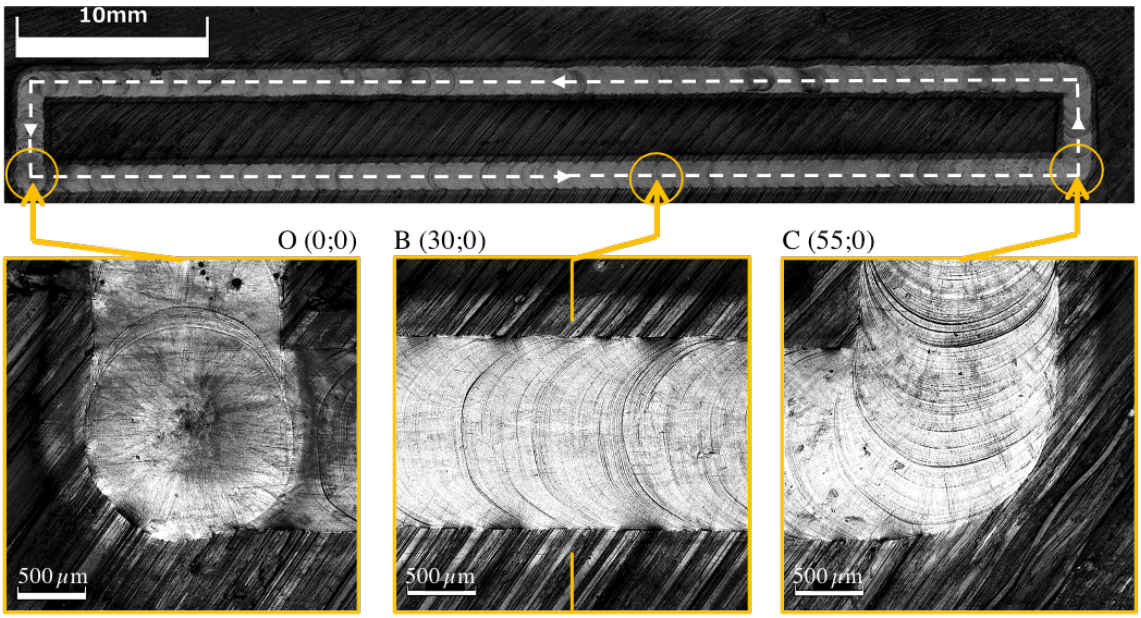

Source: Author

respectively, whereas the measured area for the melt pool mark in O (see fig.20b. for reference) was 1.93 μm^2. In this respect, and comparing the geometry of the polished track to the dimensions of the melt pool image, the pixel size was estimated in, approximately 7.10 μm.

5.2 Building DED parameters

Figure 30 presents the powder jet profile under different gases condition. In these tests, the mass flow rate ($\dot{m}$) considered was kept within the optimum range of powder delivery from the system, whereas the gas flow rates varied within the range defined by the manufacturer.

One can see in Fig. 30 the profile of powder jet at the nozzle exit. In this system, the powder flows in a channel, so there is a length measured below the laser focal point in which the powder can be caught at the melt pool – $l_{pf,i}$, where i is an integer that represents the setup number. In a similar way, the diameter in which the powder is revealed at the laser focal point was estimated, defining the variable $d_{pf,i}$.

It has been observed that, when d_{pf} is much greater than the nominal laser spot size, powder is delivered outside the melt pool region, generating powder loss and lowering the powder catchment efficiency at the melt pool. Also, delivering powder excessively to the melt pool lowers the dilution (p) once there will be more material to be melt, using the thermal energy to melt new particles other than to dilute the new layer on the previous

Figure 30 – Powder profile

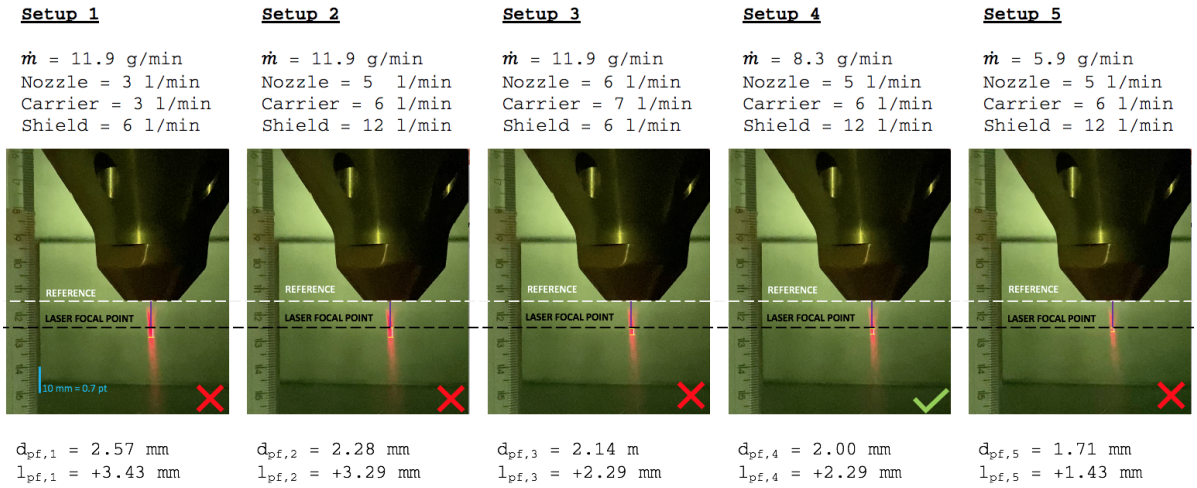

Source: Author

one. Lack of fusion can culminate from this excess of mass delivered, as a result of bad dilution, as well as layer separation. A way to balance this is to increase laser power in order to supply enough energy from melting and diluting, or reduce the mass flow rate.

In this regard, considering the laser spot size of 2 mm that can produce bead widths ranging from 1.8 to 2.2 mm, a reasonable mass flow rate would follows to that geometry when a $1.9 \leq d_{pf,i} \leq 2.1$ is aimed. Therefore, for the 3D geometry set of experiments, the powder flow rate was defined at 8.3 g/min, delivery by the conveying line of Argon gas at 6 L/min. Shielding gas at the rate of 12 L/min prevented the melt pool from oxidizing whilst the nozzle gas at the rate of 5 L/min protected the lenses on the laser head against back-flow of contaminants.

Figure 31 shows the microstructure of a good deposition, with low porosity and a typical aspect of DED with beads cross section. Some porosities are visible, which can be due to entrapped gases inside the powder, as seen in Fig.32. To this analysis, the parameters were defined to reduce porosity and promote good dilution to the substrate.

5.3 DED tests

5.3.1 Conceptual tests

As a visual result, the built geometries are shown in Fig. 33 for the monitoring only mode (Fig. 33a) and with active control on settings (Fig. 33b).

This validates that the both DTConnect and DTMap2D have succeeded in acquiring data and exposing them in an easy and straightforward way – representative of the aim of both software's concept. Due to the nature of one-track line, the visual comparison

Figure 31 – Microstructure uniformity with low percentage of pores (a) and good bead dilution to the SS304 substrate (b) at the cross-section of the SS316L block built in the contour strategy with $P = 700\ W$, $f = 600\ mm/min$ and $\dot{m} = 8.3\ g/min$. Scale: $500\mu m$.

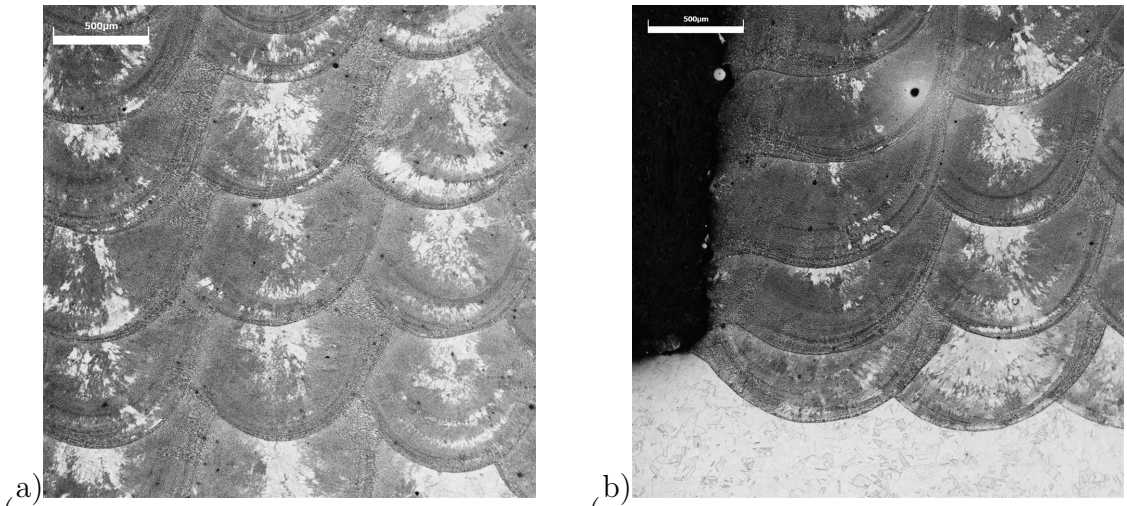

(a) (b)

Source: Author

Figure 32 – Cross-section from the 316L powder particles. Scale: $200\mu m$.

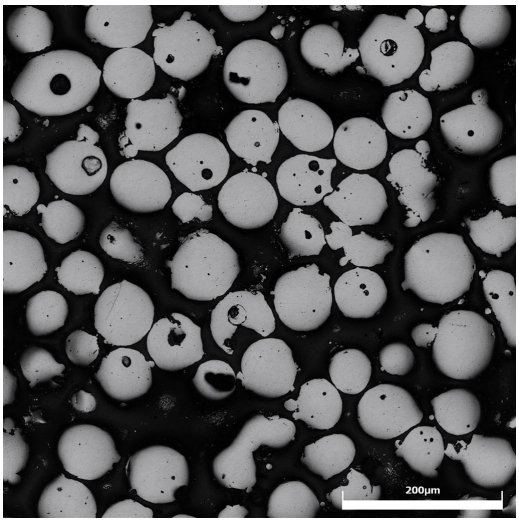

Source: Author

between the zigzag line performed with monitoring only and active feedback control on is tough to present without the aid of specific inspection tools.

By adding active feedback control to the build of a thin wall, the influence of the substrate to the first layers is considerably reduced, as shown in Fig. 56. Levels of melt pool area that are achieved in the second layer of this set would only be achieved in the

Figure 33 – Image from the zigzag line built with (a) monitoring only; and (b) active control on.

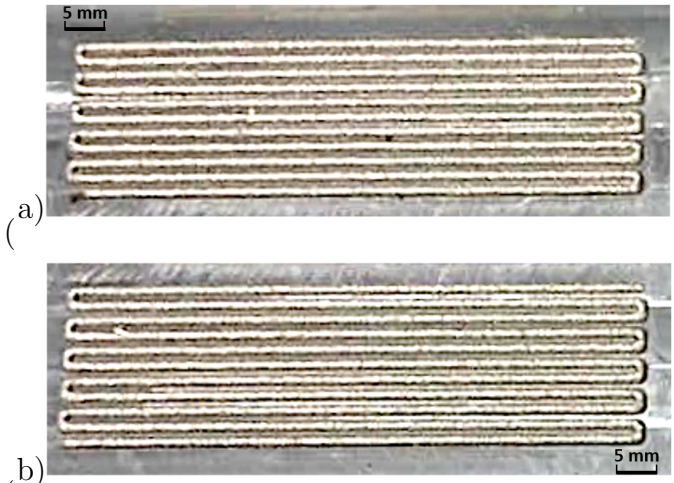

Source: Author

third layer of the build with no active feedback control; same way to the $5th$ layer from the set with feedback control, that would only be achieved at the last layer of the monitoring only set. This is a result from the adjustment of laser power during the deposition, which can also be identified at its DTMap2D graphic, reassuring that only the necessary energy will be delivered during the process.

Figure 34 – Image from the thin wall built with (a) monitoring only; and (b) active control on.

Source: Author

This effect into the part shape can be better explored in Fig. 34, which presents images from the wall printed in monitoring only mode (Fig. 34a) and with active control on settings (Fig. 34b). A rounder edge shape to the wall built with constant laser power, is representative of accumulated deviation from form due to the higher and uneven energy (added by laser plus the remained one from the previous layer) found at the melt pool and the heat transfer phenomena. With the active feedback control, this behavior can be managed towards a better part with better defined edge shape.

5.3.2 Final tests

Figure 35 presents the cross-section of the pyramids built at lower laser power at 500 W and gradient, to the contour and zigzag strategies, i.e., sets 1a, 1b, 1c and 1d, respectively.

Figure 35 – Cross-section of the pyramid built in the contour strategy at 500 W (a) and with laser power gradient (b), as well as in the zigzag strategy at 500 W (c) and with laser power gradient (d). Scale: $4mm$.

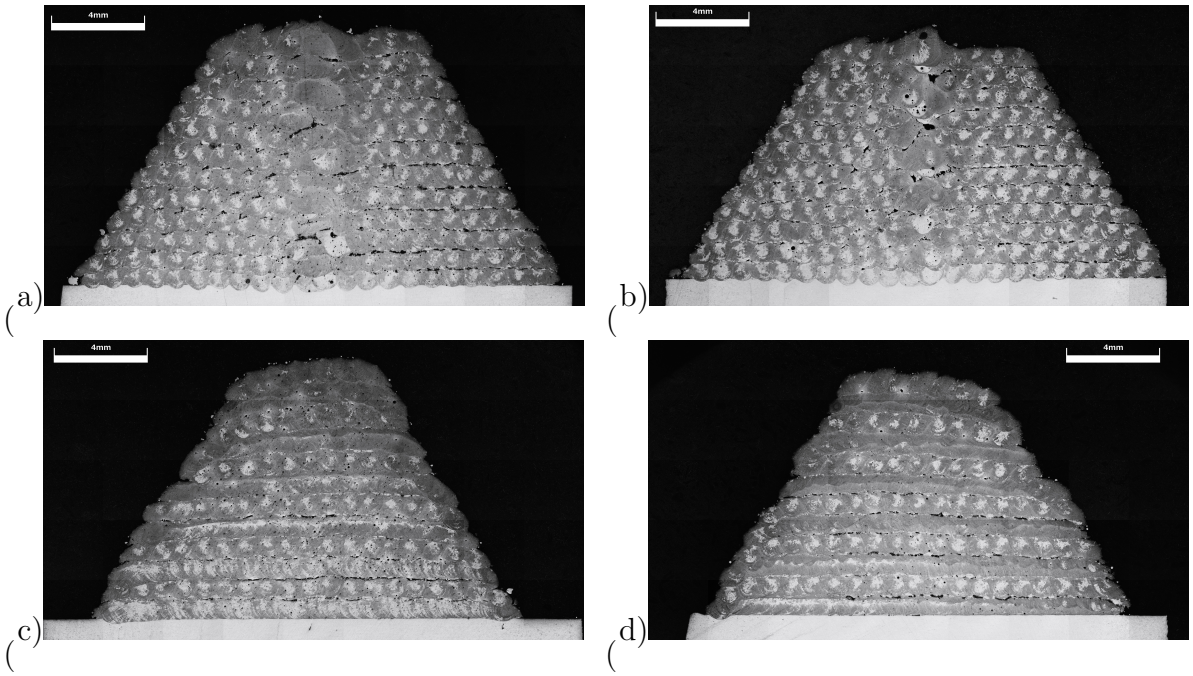

Source: Author

In all sets presented in Fig. 35, defects due to lack of fusion between beads and subsequent layers, as well as entrapped powder and pores were found. Although the sets with zigzag strategy have presented a minor amount of defects, these sets are still configuring a defected printing. In this case, a reinforced work into the build of parameters is recommended in order to increase the part internal homogeneity. Later in this section, the defects are quantified in terms of porosity percentage.

Figure 36 details some of the defects found at the cross-section of the pyramid built with contour strategy at 500 W laser power (set 1a). The appearance of these defects has shown that the energy delivered during printing was neither enough to promote the adhesion of the first layer to the substrate (see Fig. 36a), which was built with a nominally higher laser power of 550 W; nor to make a good bonding between subsequent layers (see Fig. 36b), whose are naturally build over a pre-heated bead. The presence of entrapped powder (see Fig. 36c) also relates to the delivery of insufficient energy to melt the powder at the melt pool and the previous layer, at a minimum range to promote layer dilution.

Figure 36 – Defects presented at the cross-section of the pyramid built with contour strategy and 500 W laser power (set 1a): (a) bad dilution, (b) lack of fusion, (c) entrapped powder and (d) porosity.

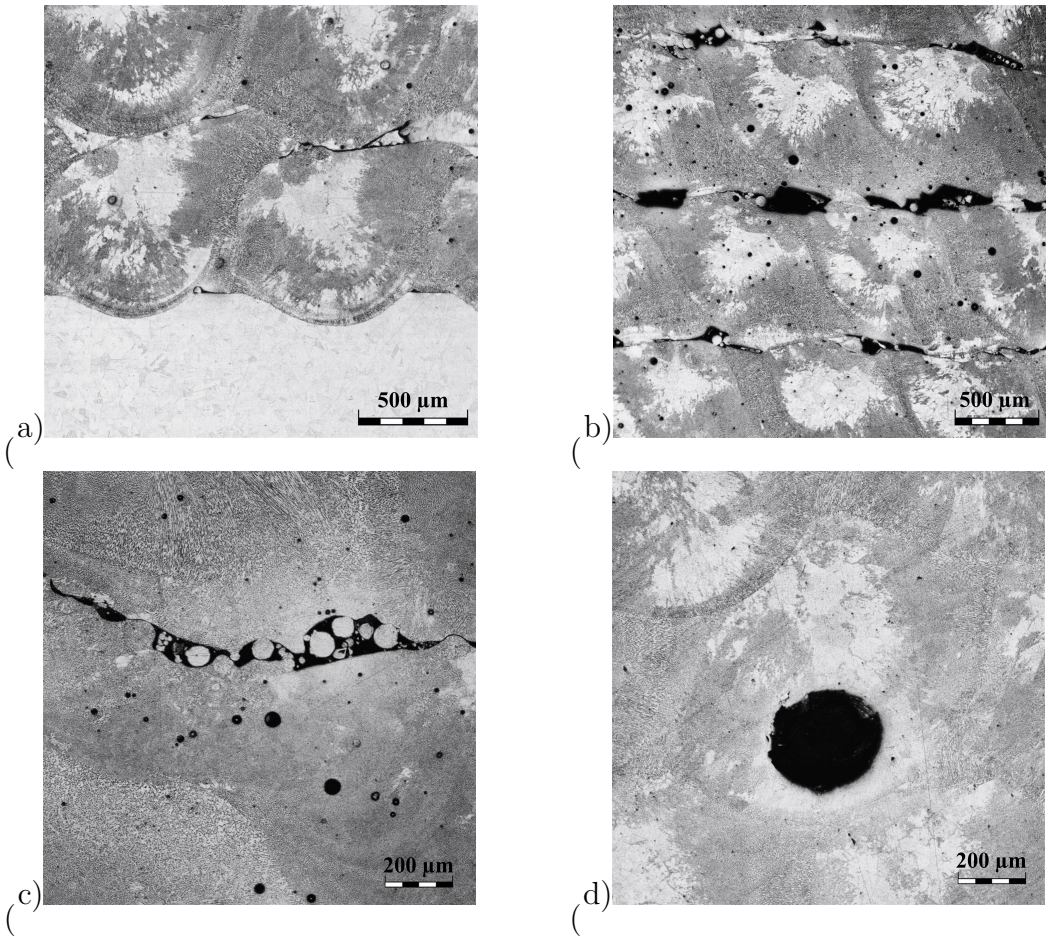

Source: Author

Last but not least, pores were highly present in this microstructure as a possible result of melt pool solidification shrinkage.

The average of porosity in each pyramid sample in both combinations of laser power and scanning strategy are shown in Fig. 37. One can see that the set considering lower laser power, regardless the printing strategy, has presented higher porosity than the other sets, that for instance were produced with 700 W and its gradient.

The pyramid built with gradient $550 - 450$ W in zigzag strategy has presented the higher percentage of porosity, estimated in 2.76%, whilst the set with 500 W produced the lowest (1.36%) from this set with 500 W. The percentage of porosity has decreased considerably (at least 5 times) with the increase of laser power to 700 W and its gradient. To the higher laser power set, it has also been observed an increase in porosity of, approximately, 60% when performing printing with laser power gradient. This implies that

Figure 37 – Porosity percentage from the pyramid builds against test condition in terms of scanning strategy and laser power.

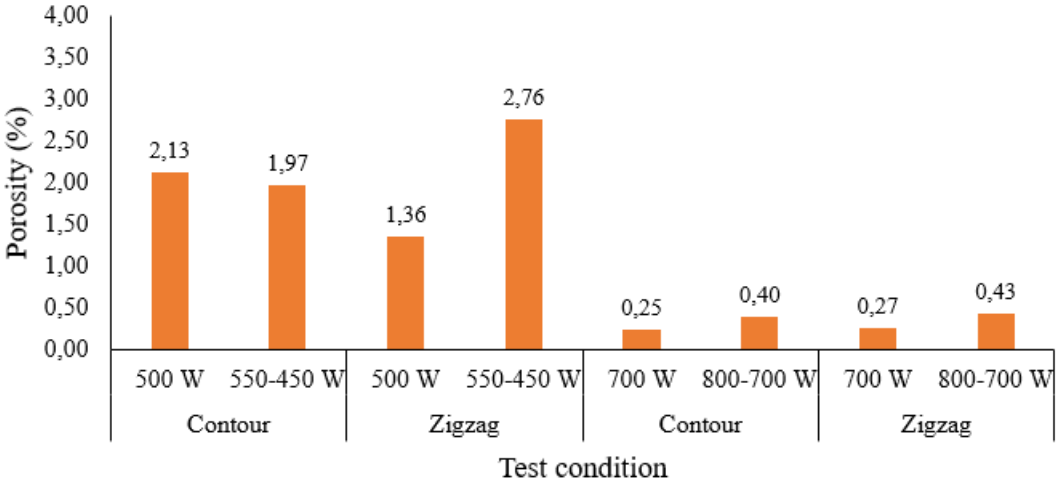

Source: Author

using a higher laser power to the first layer of the build is effective once the substrate works as a 'heat sink', however slightly decreasing the laser power through the first five layers will not have an outstanding effect into the porosity percentage, when comparing it to the samples that keeps the laser power constant from the second layer on.

Figure 38 – Pore area distribution from the pyramid builds in contour and zigzag strategies with (a) 500 W and gradient and (b) 700 W and gradient.

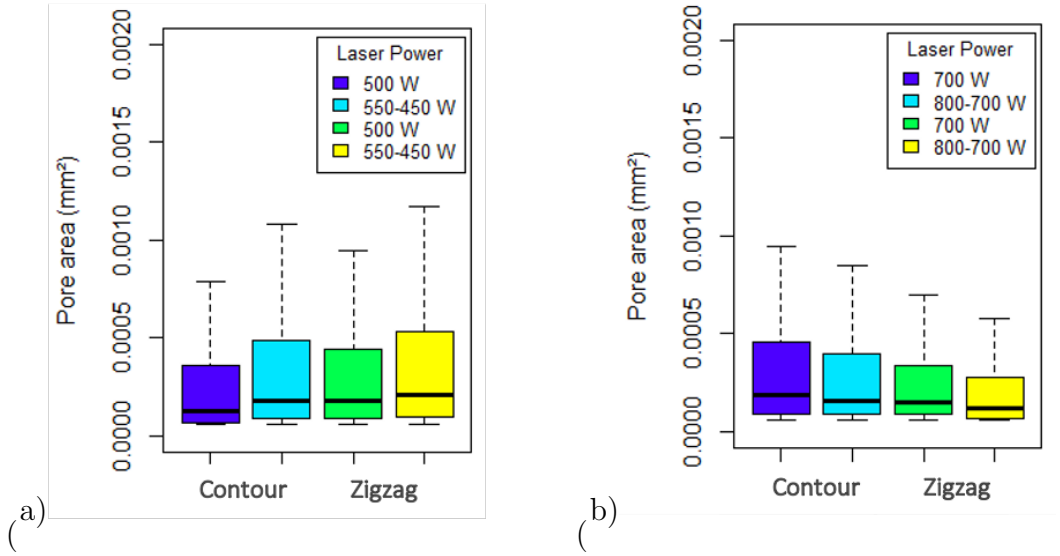

Source: Author

By evaluating the pore size (mm^2) distribution from the pyramids built, as presented in Fig. 38, one can infer about the predominance of pores and lack of fusion within the

Figure 39 – Cross-section of the pyramid built in the contour strategy at 700 W (a) and with laser power gradient (b), as well as in the zigzag strategy at 700 W (c) and with laser power gradient (d). Scale: $4mm$.

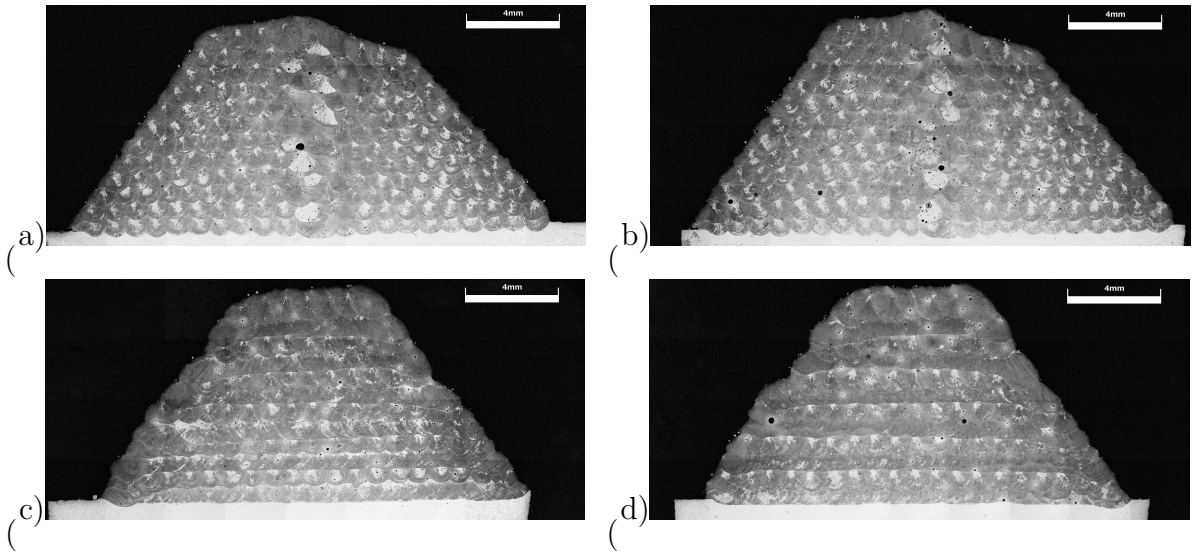

Source: Author

samples. In this scenario, higher area pores indicates lack of fusion defect, whilst minor pore areas are related to pores due to entrapped gas, and weak powder quality. Thus, the sets with higher presence of lack of fusion were the contour and zigzag with gradient laser power (550 to 450 W) whilst a decrease in this defect has been estimated with the increase in laser power (see Fig. 38b). These results can also be observed in Fig. 39, which presents images from the cross-section of the pyramids built with higher laser power (700 W and gradient), regarding the contour and zigzag strategy (i.e., sets 3a, 3b, 3c and 3d).

With the increase in laser power, the energy delivered at the melt pool has increased in 40 %, being enough to significantly enhance the quality and homogeneity in both printing strategies parts. Defects presented before, such as bad dilution, lack of fusion and entrapped powder were highly mitigated. Pores were reduced even though they are still present. This can lead to powder production defects, in which the powder has already porosity inside its particles (see Fig. 32). This powder porosity could possible be reduced by increasing the energy input to the process, however, this approach is limited as the increase in energy can also lead to ablation.

The geometry of a pyramid mould brings the stair-case effect in the inner corners of the part, differently from the pyramid. Figure 40, 41, Fig. 42 and Fig. 43, present the cross-section of the pyramid mould parts built at lower laser power, set at 500 W and its gradient (550 W to 450 W), in contour and zigzag strategies, i.e., sets 2a, 2b, 2c and 2d, respectively.

In this set, overall defects that have already been seen in the pyramids build at lower laser power were found too: lack of fusion, bad dilution, and porosity. From Fig. 42 to Fig. 43, inner and outer regions of the build are presented in augmented view, in which bad dilution between layers is also highlighted. These defects are most likely to be thermal related, and so, influenced by the heat source displacement during the build.

In other words, it is feasible that the scanning strategy has affected the amount of defects in this geometry. When the geometry imposes long distances between adjacent deposition tracks, the printed layer/bead has time to cool down, so the thermal energy that remains from the previous bead deposition is lower in longer and distant trajectories, e.g. contour strategy, than when adjacent beads are build within a minimal time spare, e.g. in zigzag strategy. Thus, the contour strategy, in this case, brings less advantages and more defects to the part than when building with zigzag pathway.

Figure 40 – Cross-section of the pyramid mould built with 500 W in contour strategy, in (a) overall view, (b) outer left, (c) inner left, (d) inner right and (e) outer right views.

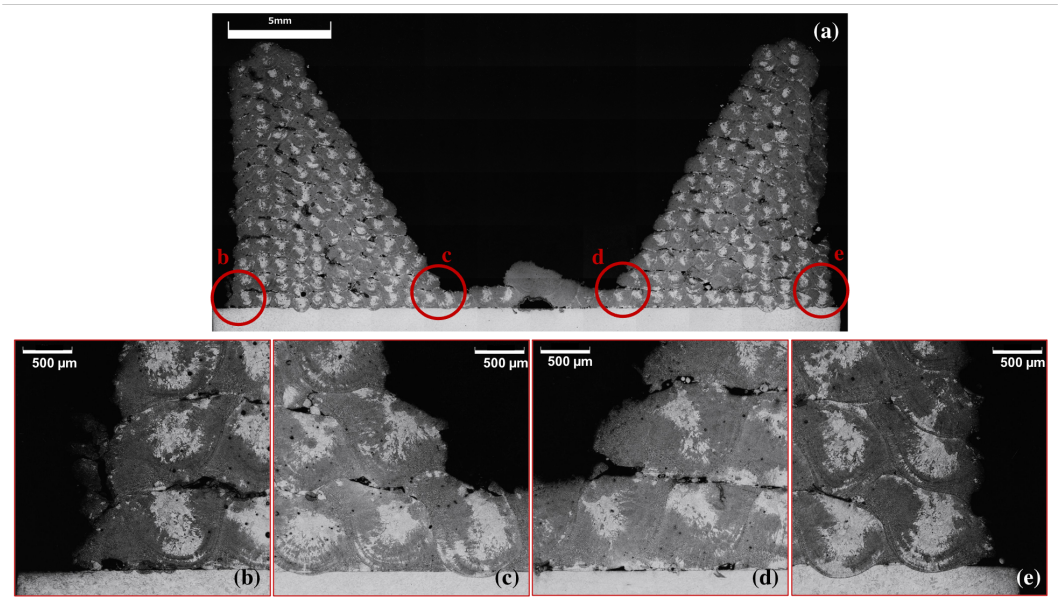

Source: Author

This is cleared when evaluating the porosity levels shown in Fig. 44, which has decreased in about 63.2 % to the set built with constant laser power and 62.7 % to the one with laser power gradient. The sets built with the same scanning strategy but different laser power configuration has presented no significant difference under the current data sets, which leads to state that building with laser power gradient does not affect the porosity levels in this geometry.

Figure 41 – Cross-section of the pyramid mould built with laser power gradient (550 W to 450 W) in contour strategy, in (a) overall view, (b) outer left, (c) inner left, (d) inner right and (e) outer right views.

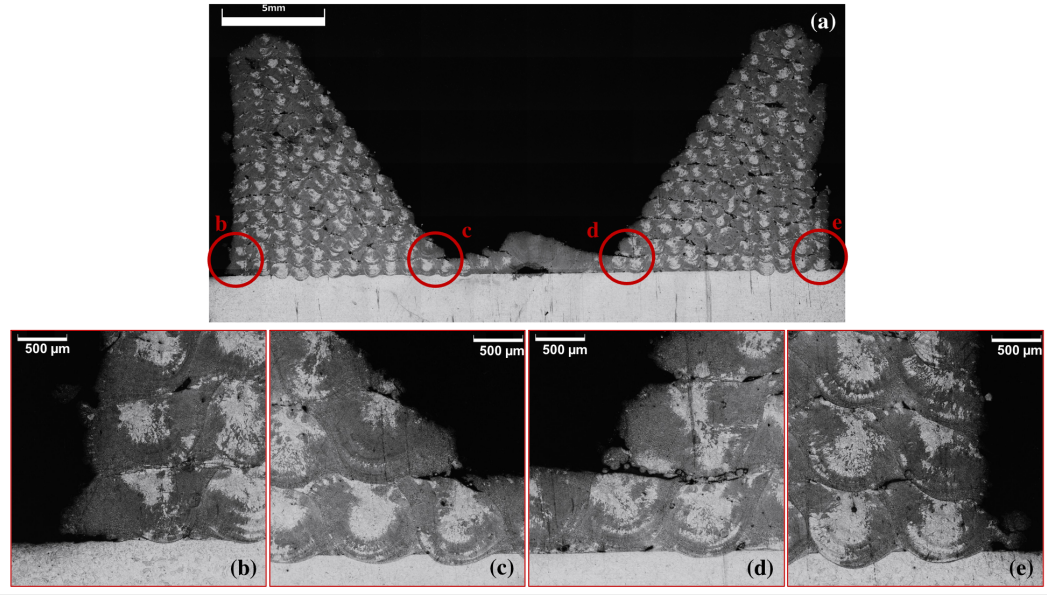

Source: Author

Figure 42 – Cross-section of the pyramid mould built with 500 W in zigzag strategy, in (a) overall view, (b) outer left, (c) inner left, (d) inner right and (e) outer right views.

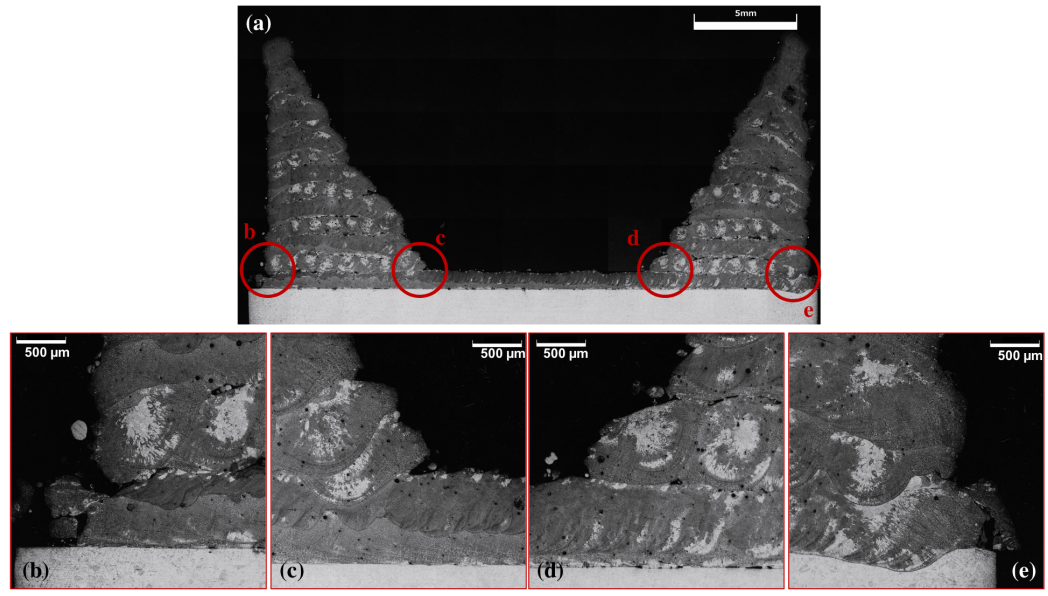

Source: Author

Figure 43 – Cross-section of the pyramid mould built with laser power gradient (550 W to 450 W) in zigzag strategy, in (a) overall view, (b) outer left, (c) inner left, (d) inner right and (e) outer right views.

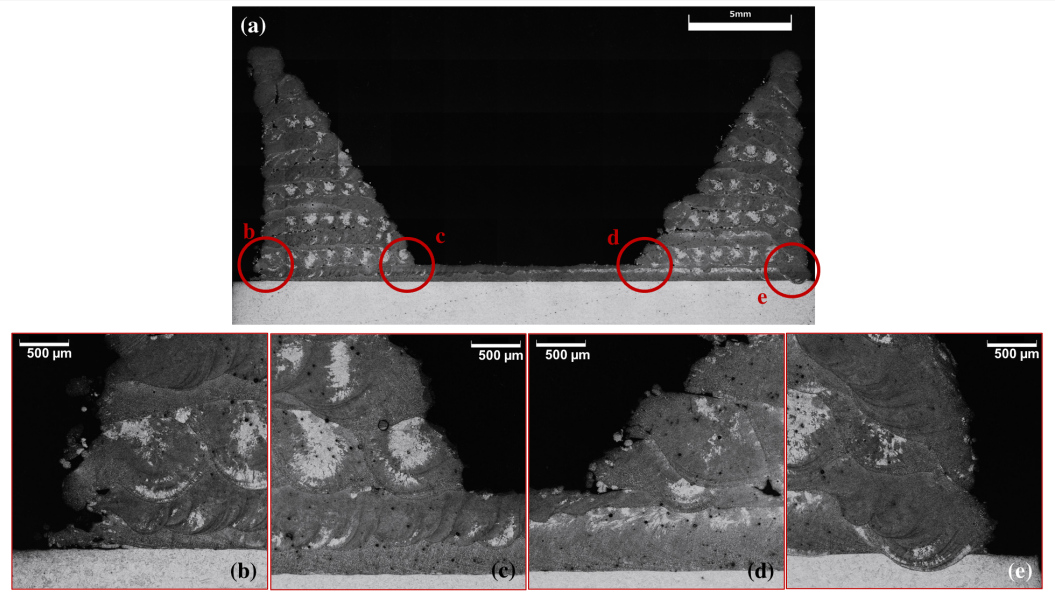

Source: Author

Figure 44 – Porosity percentage from the pyramid mould builds against test condition in terms of scanning strategy and laser power.

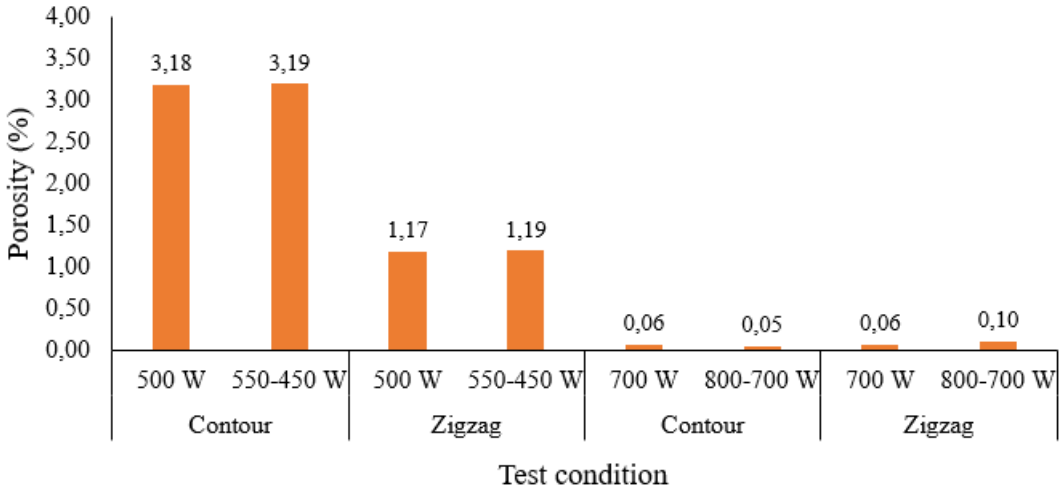

Source: Author

Figure 44 also introduces the porosity results from the set built with higher laser power. By doing so it is clear that, regardless the geometry, the reduction in terms of defects due to porosity, lack of fusion and bad dilution is strictly dependent on the energy delivered to the melt pool. Looking further into the porosity, Fig. 45 presents the pore

area distribution for the pyramid mould parts produced with lower and higher laser power.

Figure 45 – Pore area distribution from the pyramid mould builds in contour and zigzag strategies with (a) 500 W and gradient and (b) 700 W and gradient.

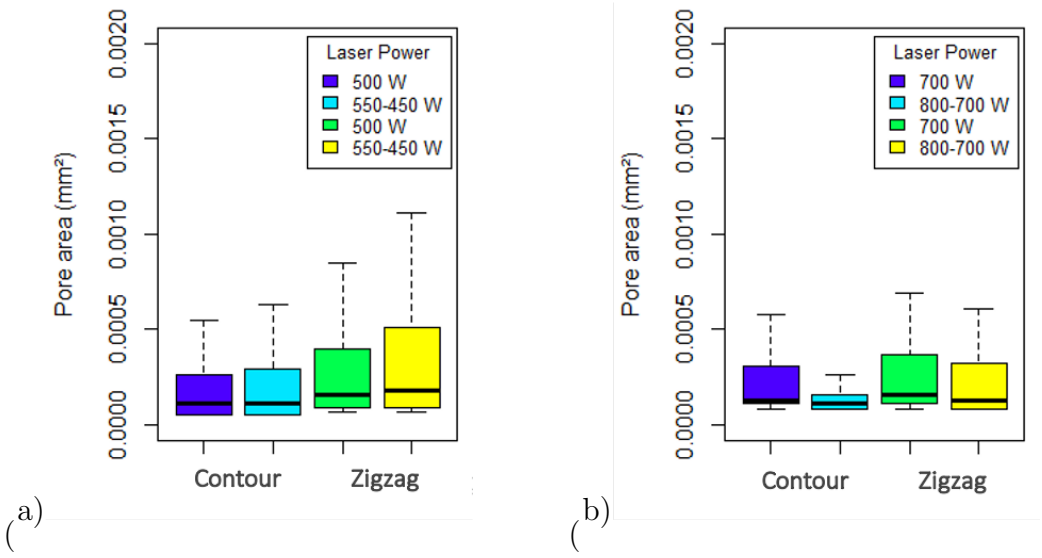

Source: Author

Likewise the data presented for the pyramid geometry (see Fig. 38), the pore area distribution indicates the presence of micro-pores, and larger pores areas that can be physically identified as regions of lack of fusion. The narrower the interval from the quarters, the most homogeneous is the structure evaluated. Thus, it is clear that contour strategy has produced more homogeneous parts at both laser power configurations, and when comparing the two levels of laser power, it is also given that overall pore size is lower to the builds produced with 700 W.

Figure 46, Fig. 47, Fig. 48 and Fig. 49 present the microstructure at the cross-section of the pyramid mould parts built under 700 W and gradient (800 W to 700 W), in contour and zigzag strategies i.e., sets 4a, 4b, 4c and 4d, respectively. From Fig. 46 to Fig. 49, inner and outer regions of the build are presented in augmented view, as well as an image of a typical microstructure showing the uniformity of the printed layers. The few defects that were present in these sets were pores most likely to be from entrapped gas or remained from powder production process.

Regarding the final geometry of the builds, a rounder top edge is found in the pyramid moulds produced by contour strategy, when compared to the final form of the parts produced in zigzag pathway. This difference was mainly noted in the sets produced at 700 W and gradient (see Fig. 46 to Fig. 49), and can be due to a loss of focus at the end of the build, adding up to the edged geometry, which is already know to have form deviation highly affect by deposition out of focus.

Figure 46 – Cross-section of the pyramid mould built with 700 W in contour strategy, in (a) overall view, (b) outer left, (c) inner left, (d) inner right and (e) outer right views.

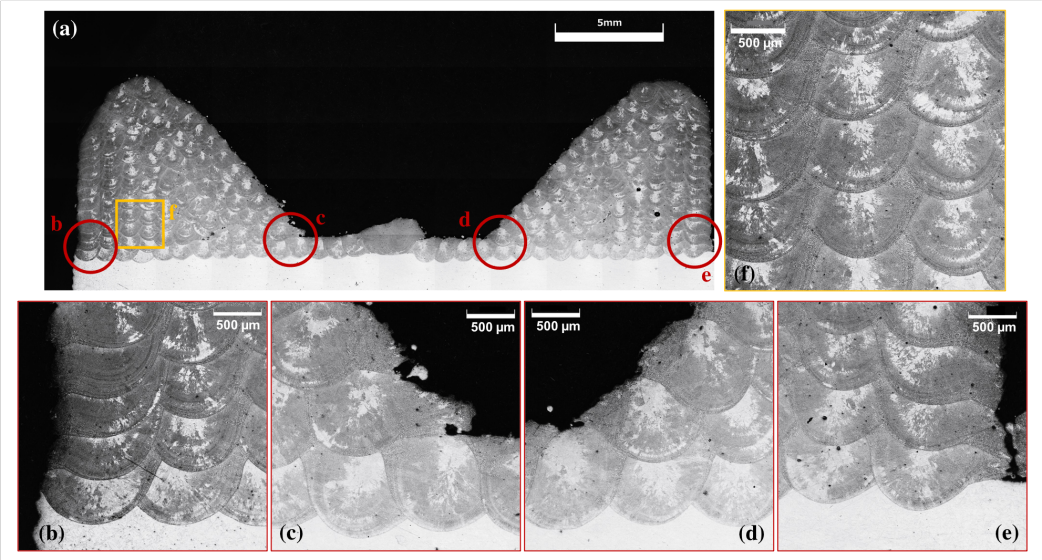

Source: Author

Figure 47 – Cross-section of the pyramid mould built with laser power gradient (800 W to 700 W) in contour strategy, in (a) overall view, (b) outer left, (c) inner left, (d) inner right and (e) outer right views.

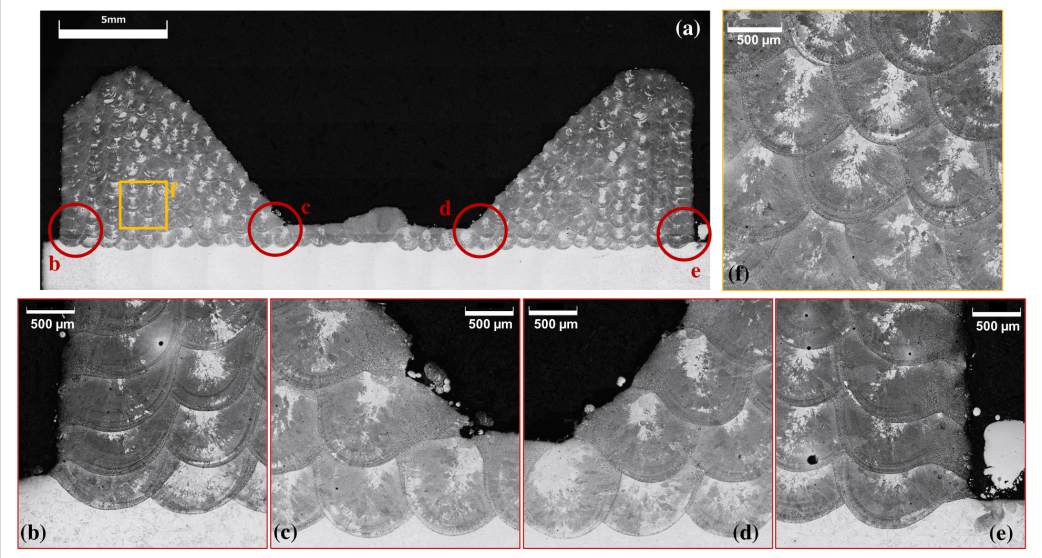

Source: Author

Figure 50 presents the parts printed with 500 W and its gradient to the different geometries and scanning strategies, as built.

Figure 48 – Cross-section of the pyramid mould built with 700 W in zigzag strategy, in (a) overall view, (b) outer left, (c) inner left, (d) inner right and (e) outer right views.

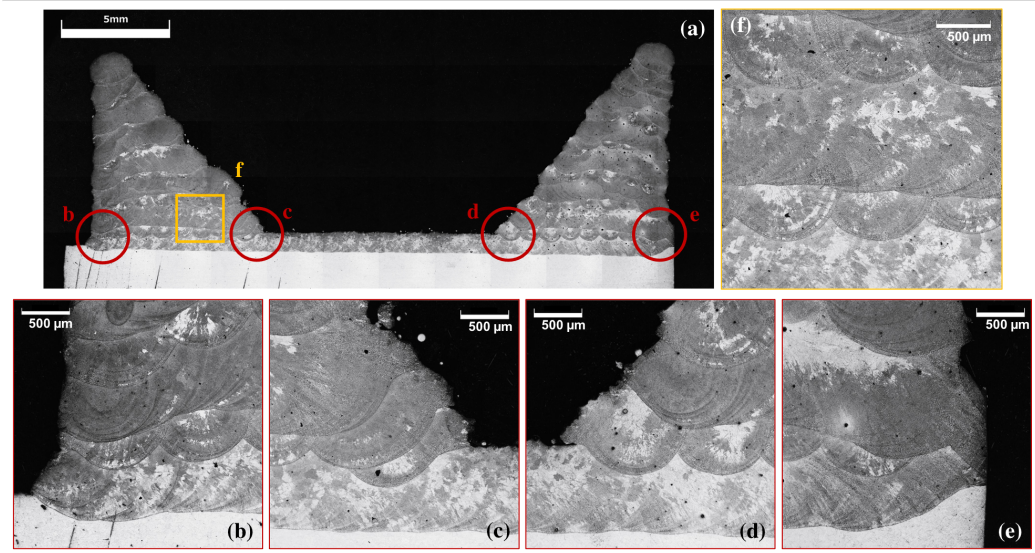

Source: Author

Figure 49 – Cross-section of the pyramid mould built with laser power gradient (800 W to 700 W) in zigzag strategy, in (a) overall view, (b) outer left, (c) inner left, (d) inner right and (e) outer right views.

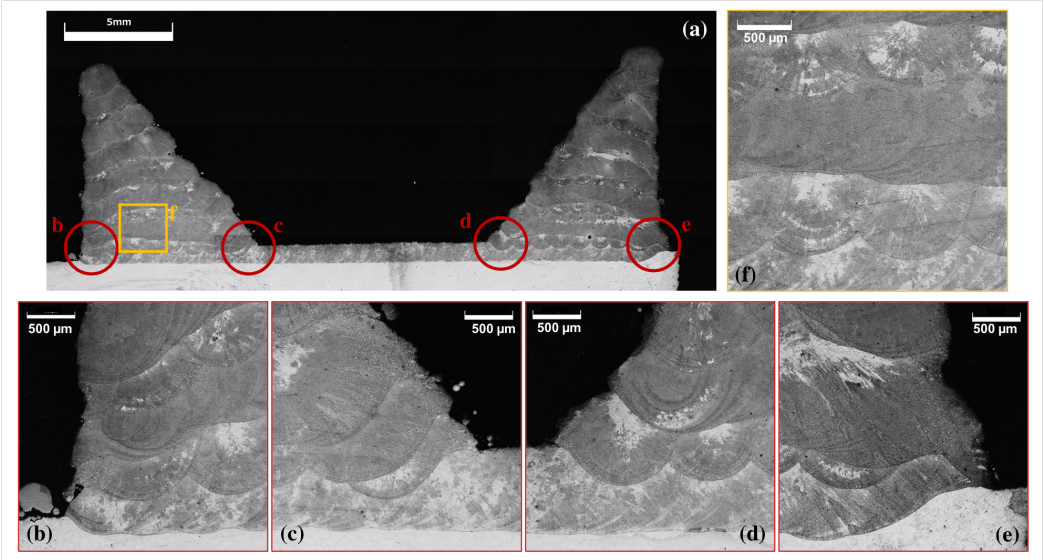

Source: Author

Figure 51 presents the parts printed with 700 W and its gradient to the different geometries and scanning strategies, as built.

Figure 50 – Image from the parts built with 500 W and gradient.

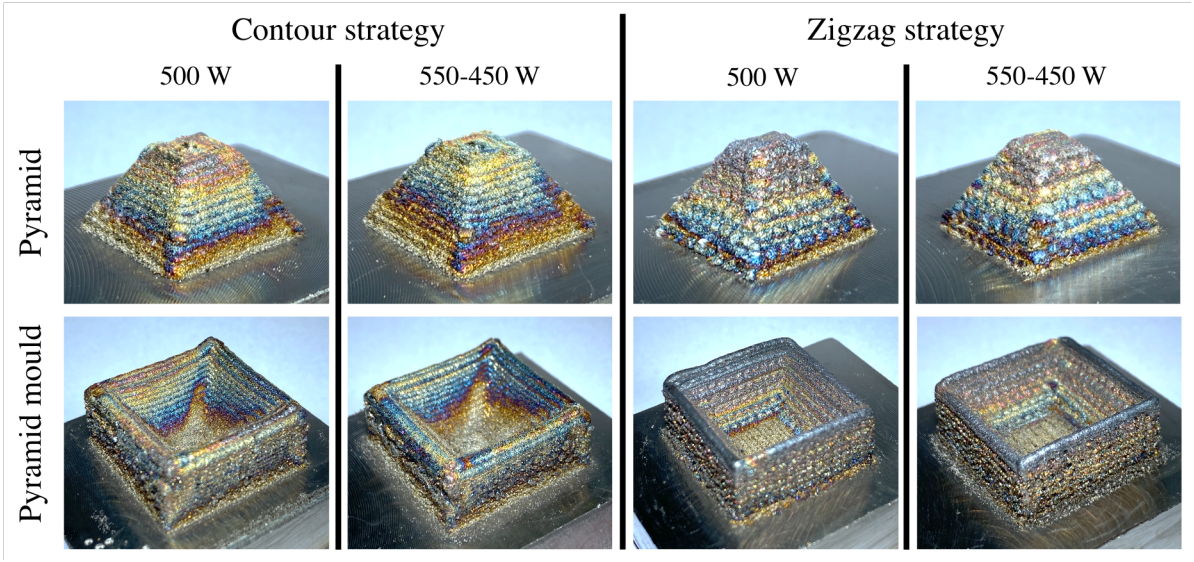

Source: Author

Figure 51 – Image from the parts built with 700 W and gradient.

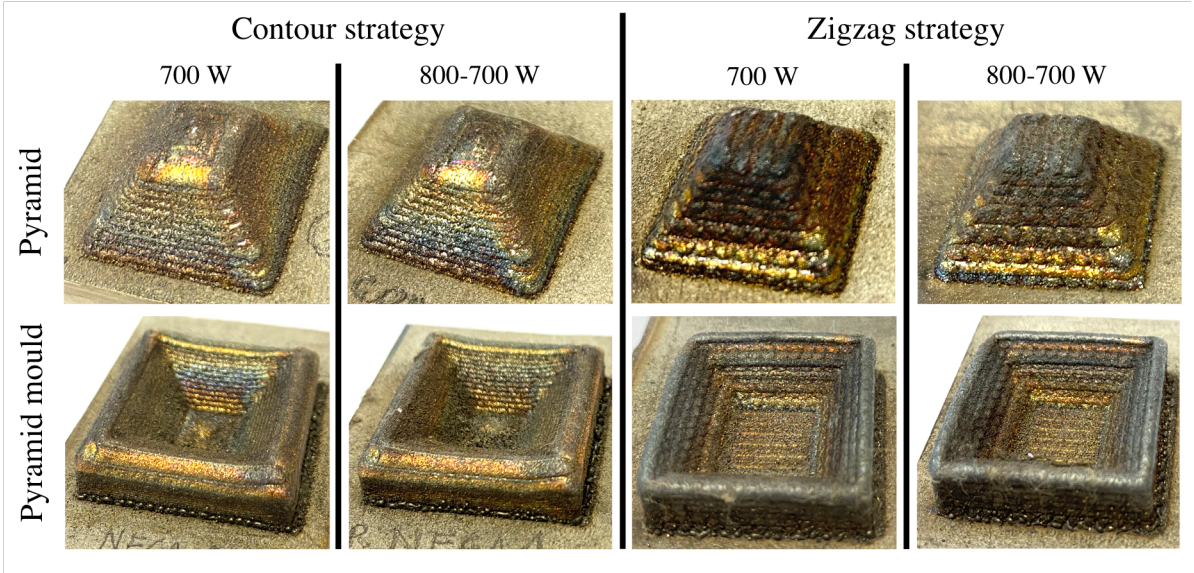

Source: Author

Figure 52 presents the assembly of the parts printed with 500 W and its gradient to the different scanning strategies, as built.

Figure 52 – Assembly of the parts built in contour strategy with (a) 500 W and (b) gradient, and in zigzag strategy with (c) 700 W and (d) gradient.

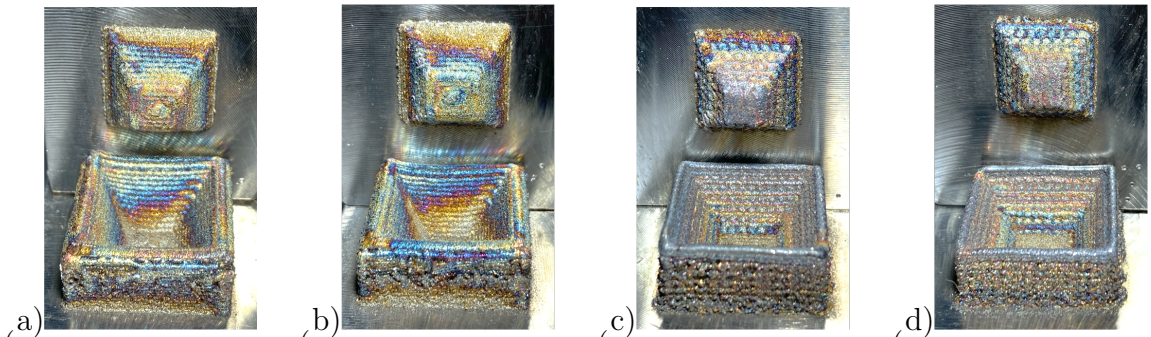

(a) (b) (c) (d)

Source: Author

5.4 Data Analysis

5.4.1 DTMap2D

The first application of the DTMap2D was during a build up of a zig-zag track. First, the wall was built without any feed back control of laser power. All data was acquired by DTConnect software and exported as CSV data to the DTMap2D, which then plotted a graph for each of the monitored parameters (laser power, feed speed and melt pool area). Figure 53 presents the monitoring data with no intervention from the controller on the laser power. To this set, the color from the DTMap is expected to be constant to the laser power, as shown. On the other hand, a higher variation to the melt pool area is expected, since the interaction between the laser power and the substrate vary due to the complex phenomena that occurs during DED operations. The feed speed is one parameter that has high influence on the produced part, which makes its monitoring imperative to the process besides laser power and mass flow rate.

The variation of feed speed in CNC machines is expected to happen during a change of motion direction (due to inertia), as well as through some readings of lines in G-code and sub programs. In this respect, when the feed speed is lower than the programmed, more material will be delivered at that specific region, introducing variability of layer height to the build. The same defect can occur when a higher feed speed is obtained during deposition, generating a lower layer height in this case. The DTMap2D for feed speed has identified a decrease in the feed speed at the corners of the zigzag toolpath, leading to a gain of material thus a higher layer height at these turnabouts.

By adding a feedback control to adjust the laser power within the specified range of melt pool area, the deposition rate can be influenced by the melt pool shape. Figure 54 shows the plot for the same parameters (laser power, feed speed and melt pool area),

Figure 53 – DTMap2D plot of (a) laser power; (b) feed speed; and (c) melt pool area from the build of a zigzag track with no active feedback control (monitoring only).

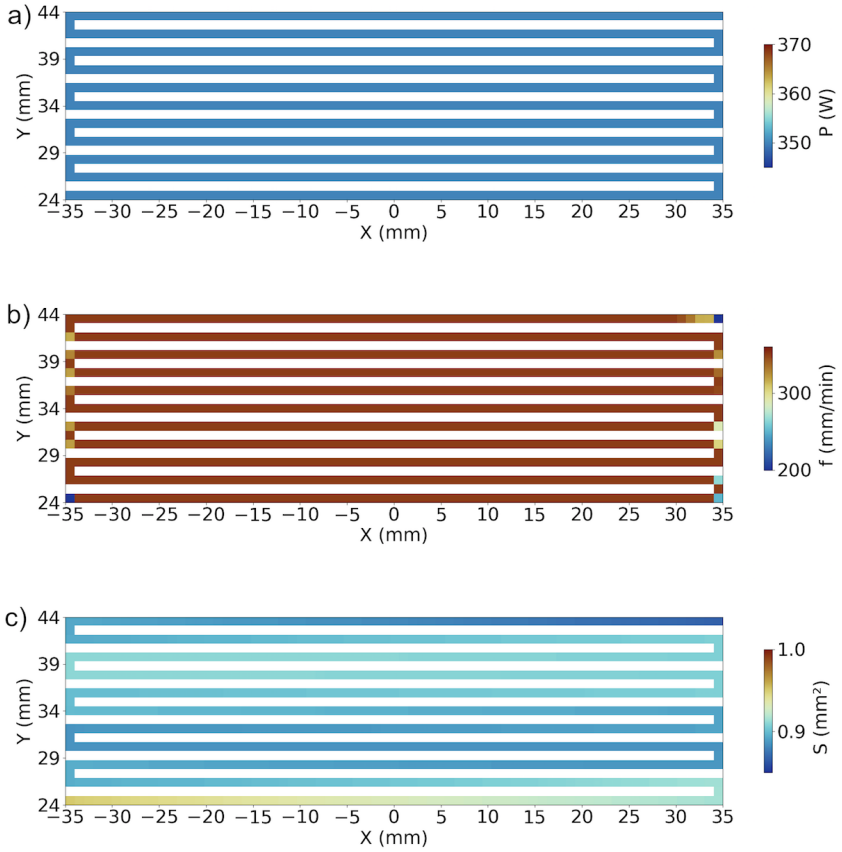

Source: Author

now with a feed back control 'ON'. In this case, the change in laser power is shown in the plot, which can be beneficial for identifying defects and failure in future applications of DTMap2D.

As for the feed speed, there was no substantial change from the results aforementioned since the G-code from both sets of zigzag track geometry is the same. This culminates in a highly reproducible behavior on the position and motion from the CNC. Last, but not least, the melt pool area and shape will also have significant changes during the process, as it also varies with laser power and the in-process powder capture efficiency by the melt pool.

The deposition of a thin wall increases the challenges during the building and the inspection due to the accumulative effect of the reheating cycles – which has higher influences on the melt pool parameters, thus to the final layer height (assuming that the powder capture efficiency at the melt pool remains constant during deposition). Figure 55 presents the monitored data from the build of a thin wall with no feedback control.

Figure 54 – DTMap2D plot of (a) laser power; (b) feed speed; and (c) melt pool area from the build of a zigzag track with active feedback control on.

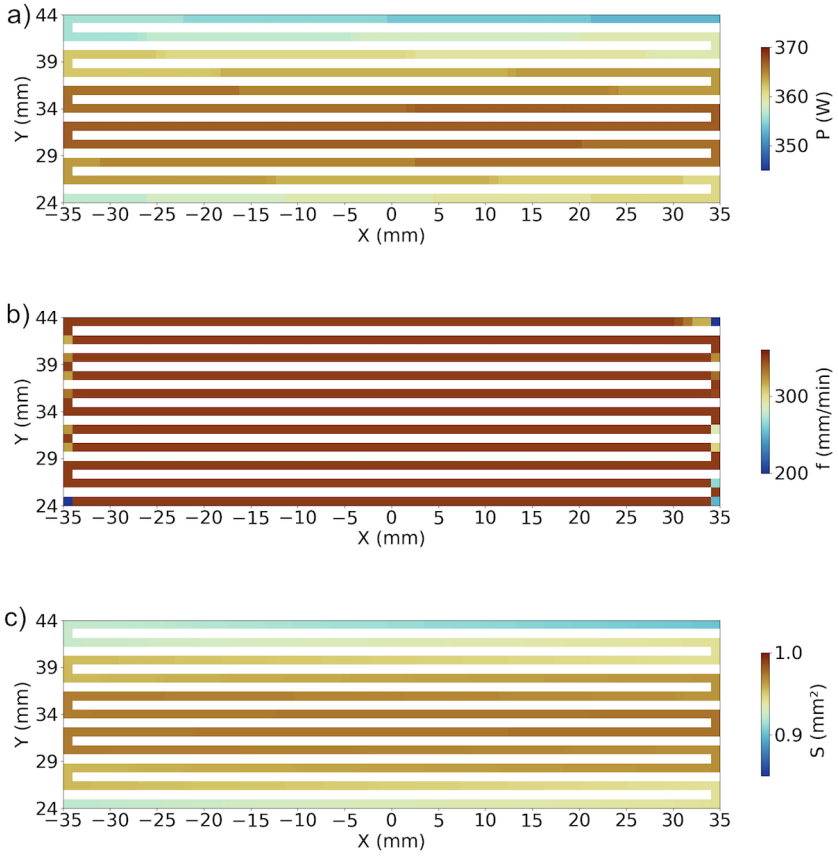

Source: Author

In Fig. 55, there is no variation in laser power and, as for the feed speed, there is some at the end of each deposited line. This variation in the feed speed data is expected from the CNC machine, once it will slow down at the end of each layer for increasing the height for the build of the following line. The melt pool area is shown to be lower at the first layers.

This is found because the substrate (at room temperature) dissipates energy, which tends to create a smaller melt pool area. As the wall becomes higher, the following layers no longer experiences a high temperature difference, but preheated material that would still carry energy from the last built line, in favor of higher melt pool area generation.

Regarding these two setups, both DTConnect and DTMap2D concepts and applications were presented and validated. DTMap2D has been shown to be a feasible tool for visualizing captured data, and DTConnect to capture and export data and monitor the CNC activity (including from the DED processes in this case). This makes the DTMap2D a potential tool to speed up the identification of critical regions for post-build inspection. It also makes the visualization and the interpretation of data collected easier. This can lead

Figure 55 – DTMap of (a) laser power; (b) feed speed; and (c) melt pool area from the build of a thin wall with no active feedback control (monitoring only).

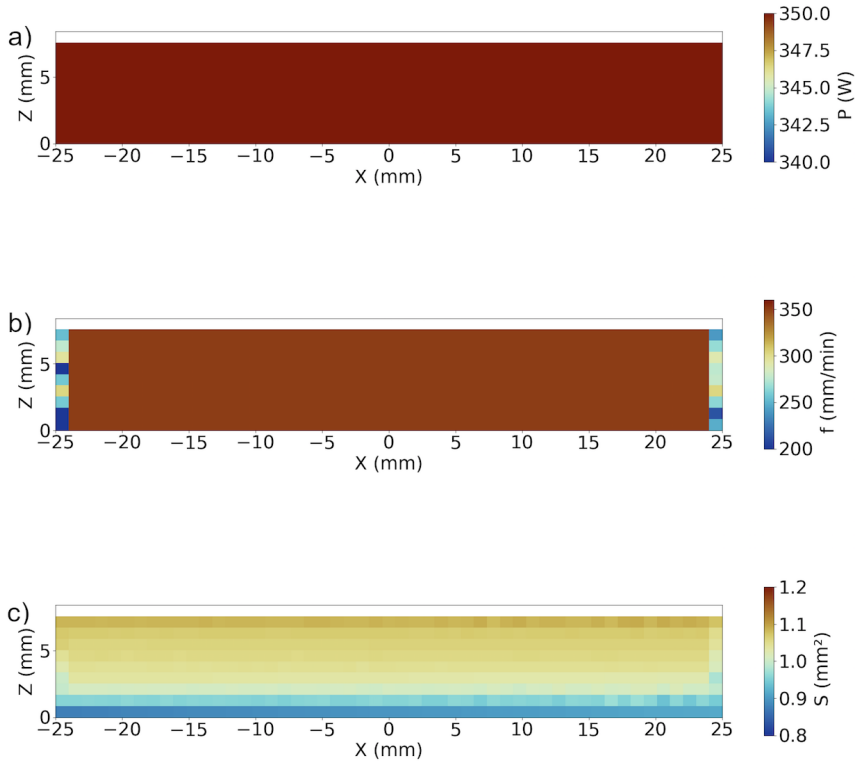

Source: Author

to faster identification of builds that are experiencing difficulty and that need operator intervention.

Overall, these experiments have illustrated one possible use of these collection and visualization tools. The base concepts to the development of these software tools can also be used for a wide variety of processes when paired with appropriate sensors, data collection, and automatic error detection algorithms. These concepts were imperative for the development of the DTMap3D, discussed on the following section.

Figure 56 – DTMap2D plot of (a) laser power; (b) feed speed; and (c) melt pool area from the build of a thin wall with active feedback control.

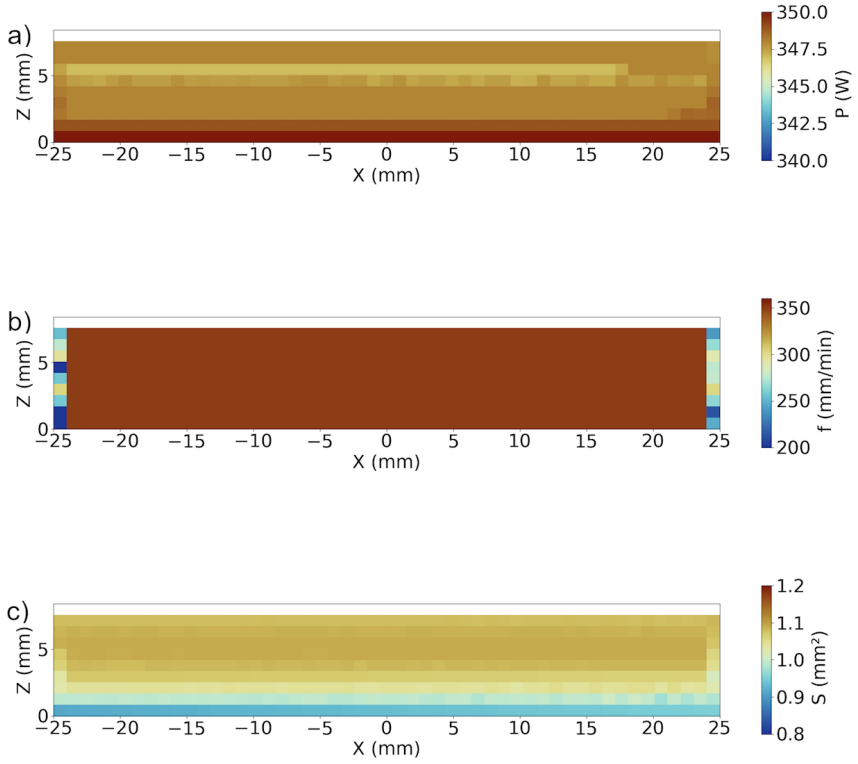

Source: Author

5.4.2 DTMap3D

Figure 57 presents the DTmap3D for the feed speed as the monitoring data acquired during the pyramids built at 500 W and gradient by contour and zigzag strategies, in isometric view. As one can see, there is no much difference from the sets with laser power gradient to the ones with constant laser power. Although minor differences were achieved during the toolpath performance, feed speed is highly influenced by the scanning strategy and independent from laser power. This adds up to the variation in heat distribution that the scanning strategy brings to the building, making zones with reduction in feed speed potential zones of higher bead height, and deviation from form by consequence.

Furthermore, regarding the contour and zigzag strategies, both presents zones of reduction in feed speed. To the contour, these zones are located in the corners from each square loop, while presented at every single bead border in zigzag trajectories – both particularities shown clearly in Fig. 57. The major outcome from this parameter deviation is the potential height fluctuation in borders (zigzag). This influences the part surface roughness, in zigzag strategy, and only corners to contour strategy. Thus, when considering printing pyramids in contour, variation in feed can bring to the part form defect in borders

Figure 57 – DTMap3D plot of feed speed from the pyramids sets built by contour at (a) 500 W and (b) gradient, and by zigzag at (c) 500 W and (d) gradient.

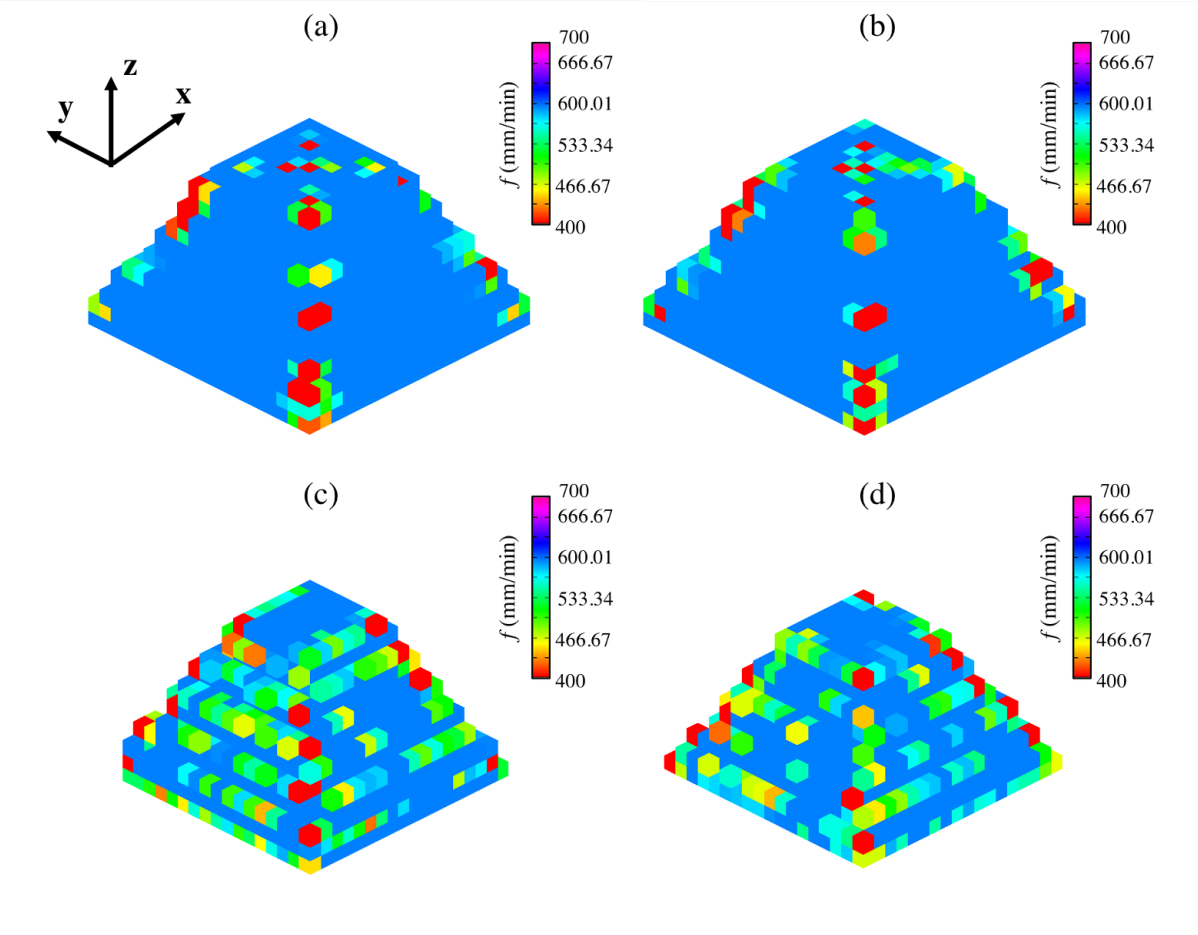

Source: Author

although the part may present better surface finishing when compared to the one produce by zigzag strategy. In both cases, the parts finishing will be affected by the stair-case effect.

Figure 58 presents the DTmap3D for the feed speed as the monitoring data during the pyramids built at 700 W and gradient, by contour and zigzag strategies, in isometric view. As shown, similar results were achieved when compared to the ones presented in Fig. 57. This is due to the fact that these sets do not vary in terms of feed configuration, only in therms of laser power. Also, this is valid to pose that the machine kinematics has great repeatability.

Figure 58 – DTMap3D plot of feed speed from the pyramids sets built by contour at (a) 700 W and (b) gradient, and by zigzag at (c) 700 W and (d) gradient.

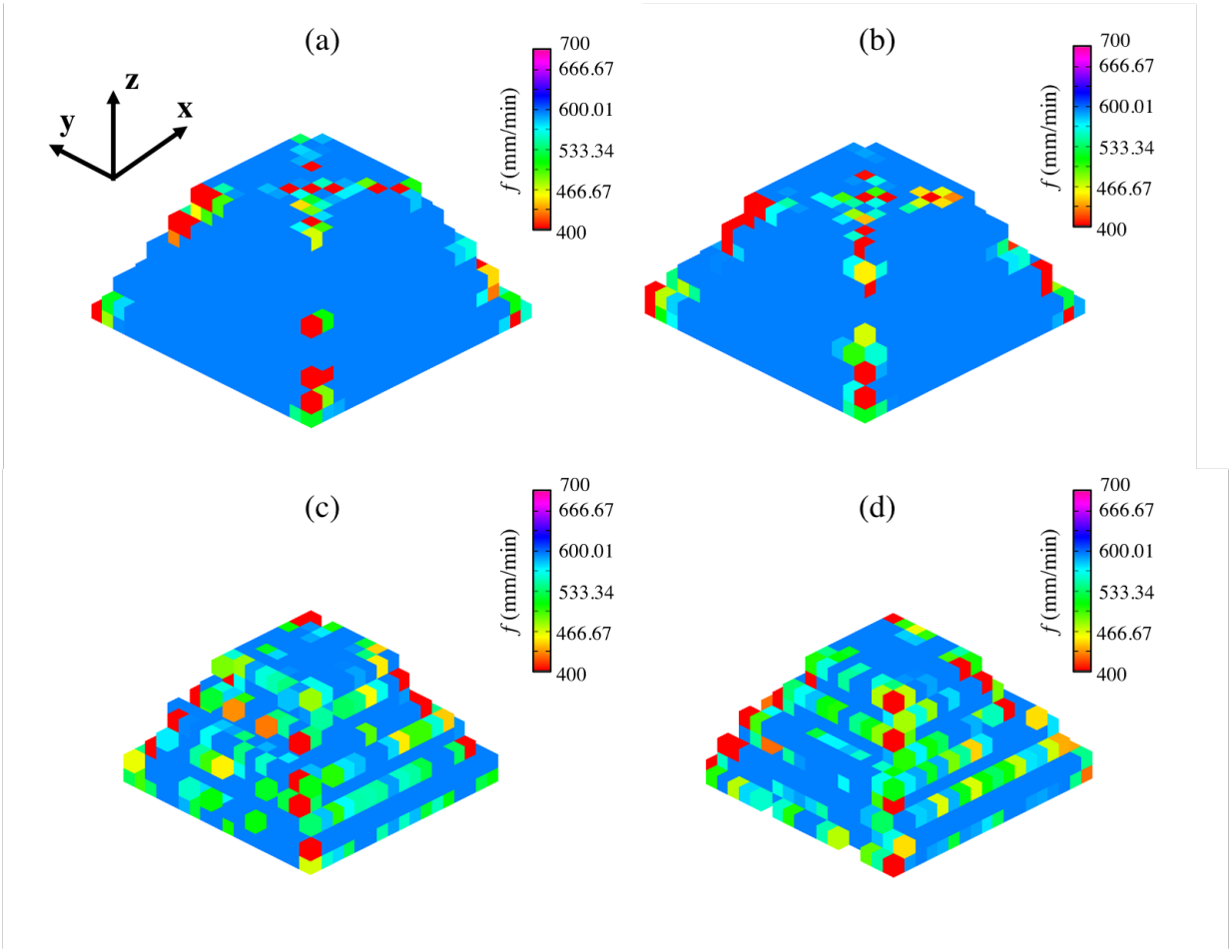

Source: Author

Figure 59 presents the spot area from the melt pool as the monitoring data acquired during the pyramids built at 500 W and gradient by contour and zigzag strategies, in the xz-plane at $y = 10$. The data presented shows an average spot area around 3.5 mm^2, whilst higher and lower values are observed at the plots cross-sections.

Higher levels of melt pool area were reached at the higher laser power set, as shown in Fig. 60. Figure 60 presents the spot area from the melt pool as the monitoring data acquired during the pyramids built at 700 W and gradient by contour and zigzag strategies, in the xz-plane at $y = 10$.

The data presented in Fig. 60 shows a higher variation in the melt pool spot area measurements. Lower spot area is expected to take place in the first layers as a result from the heat dissipation process to the substrate. The higher the lase power, the higher the energy delivered in setups with feed speed and mass flow rate steady. As the print goes up, the melt pool spot area may vary at the borders, once the plane for back-reflecting

Figure 59 – DTMap3D plot of spot area from the pyramids sets built by contour at (a) 500 W and (b) gradient, and by zigzag at (c) 500 W and (d) gradient, at the xz-plane for Y=10.

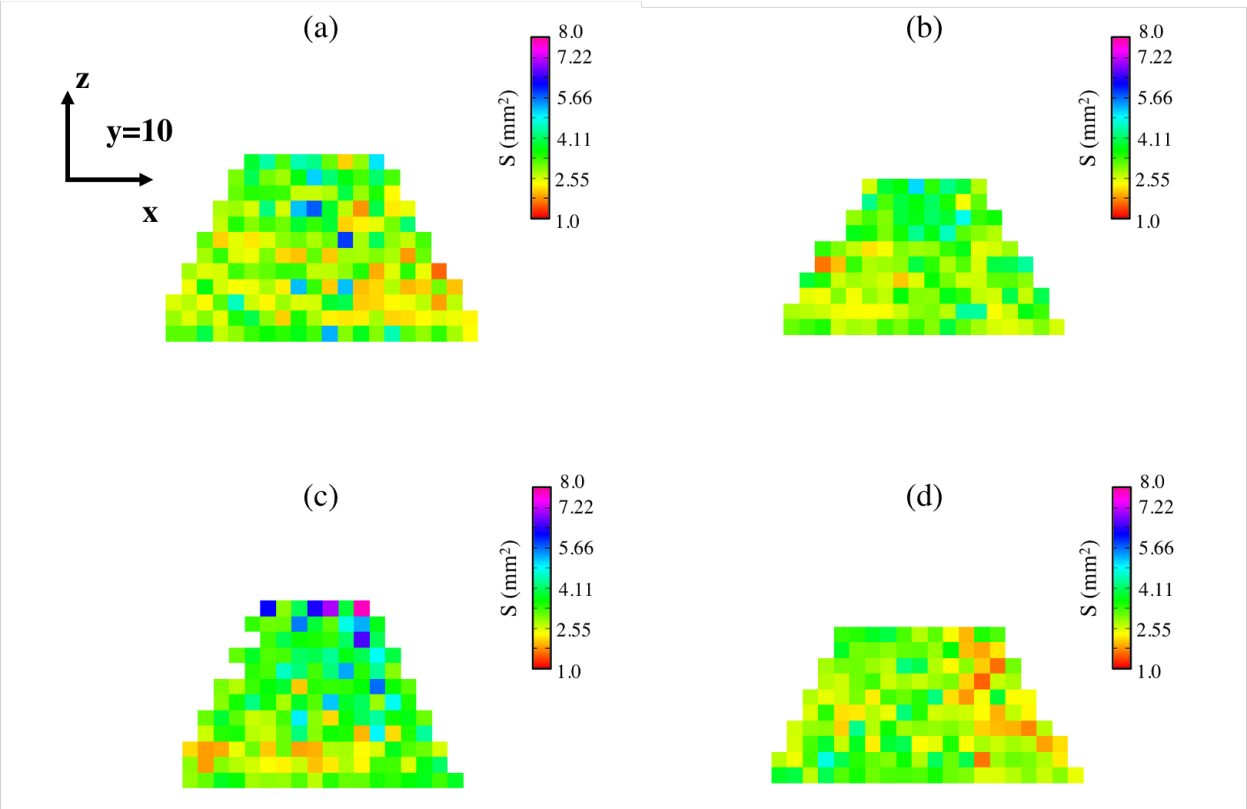

Source: Author

the light to the camera can be highly influenced by the stair-case effect.

Also, zones with a very high melt pool spot area, mainly presented in Fig. 60c. and Fig. 60d., can also represent regions in which the deposition had occurred out of focus. The reason for this regards the methodology for image processing developed in this research, that allows zones of lose focus to be identified. Such a feature is possible because the higher the distance between laser and camera focus, the blurrier the image formed at the camera; so a minor amount of light intensity reaches the system, bringing the OTSU's threshold to a lower level. That directly affect the adaptive threshold used to the image processing stage adopted here. Thus, the binary image presents a higher region of white pixels than the usual, and although this mislead the area of the melt pool, it actually indicates a region that the focus is lost. When considering a calibration to quantify how far the deposition is of its focus by means of how the adaptive threshold and the layer height produced under different Z-offset circumstances are related, this method and map can also be used for feed-back information that can adjust the z-layer increment between layers to prevent deposition out of focus to occur.

Figure 60 – DTMap3D plot of spot area from the pyramids sets built by contour at (a) 700 W and (b) gradient, and by zigzag at (c) 700 W and (d) gradient, at the xz-plane for Y=10.

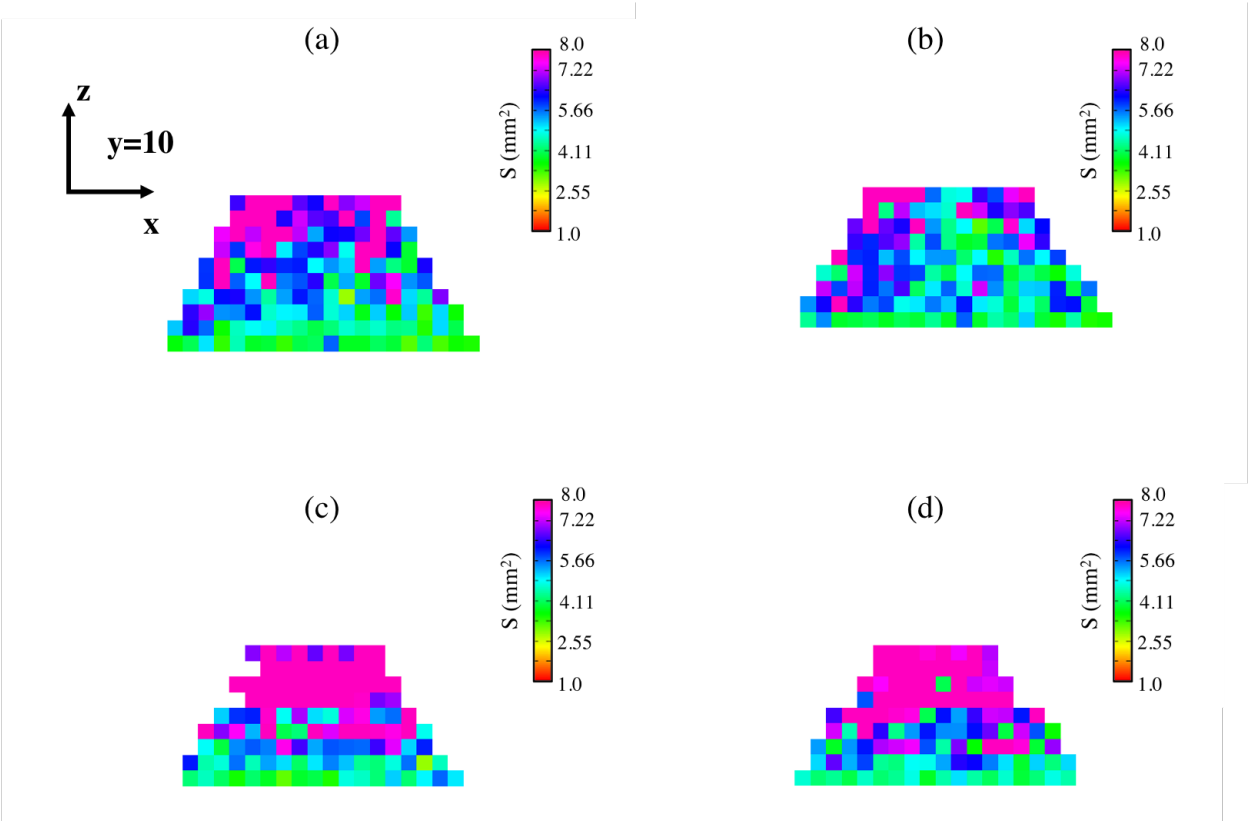

Source: Author

Figure 61 and Fig. 62 present the laser power as the monitoring data acquired during the pyramids built at 500 W and gradient by contour and zigzag strategies, in the xz-plane at $y = 10$, and at 700 W and gradient by contour and zigzag strategies, in the xz-plane at $y = 10$, respectively.

In all sets, the laser power configuration tends to remain constant during the deposition, unless in points that it is starting or shutting from firing, or when programmed to vary every layer. By considering the contour strategy, laser starts at the beginning of each bead, and shuts down at the end of each one, allowing the head can move to the starting point of next bead without depositing material. This is the reason why some laser variation is found at the center of the pyramids build by contour, in both laser configurations (see Fig. 61a., Fig. 61b, Fig. 62a. and Fig. 62b).

Big size pores and lack of fusion were observed in the pyramids built by contour strategy sets with 500 W (see Fig. 35a.) and its gradient (see Fig. 35b.), and 700 W (see Fig. 39a.) and its gradient (see Fig. 35b.). Although further studies must be done towards this defect-parameter relationship, the presence of high area pores and lack of fusion is

Figure 61 – DTMap3D plot of feed speed from the pyramids sets built by contour at (a) 500 W and (b) gradient, and by zigzag at (c) 500 W and (d) gradient.

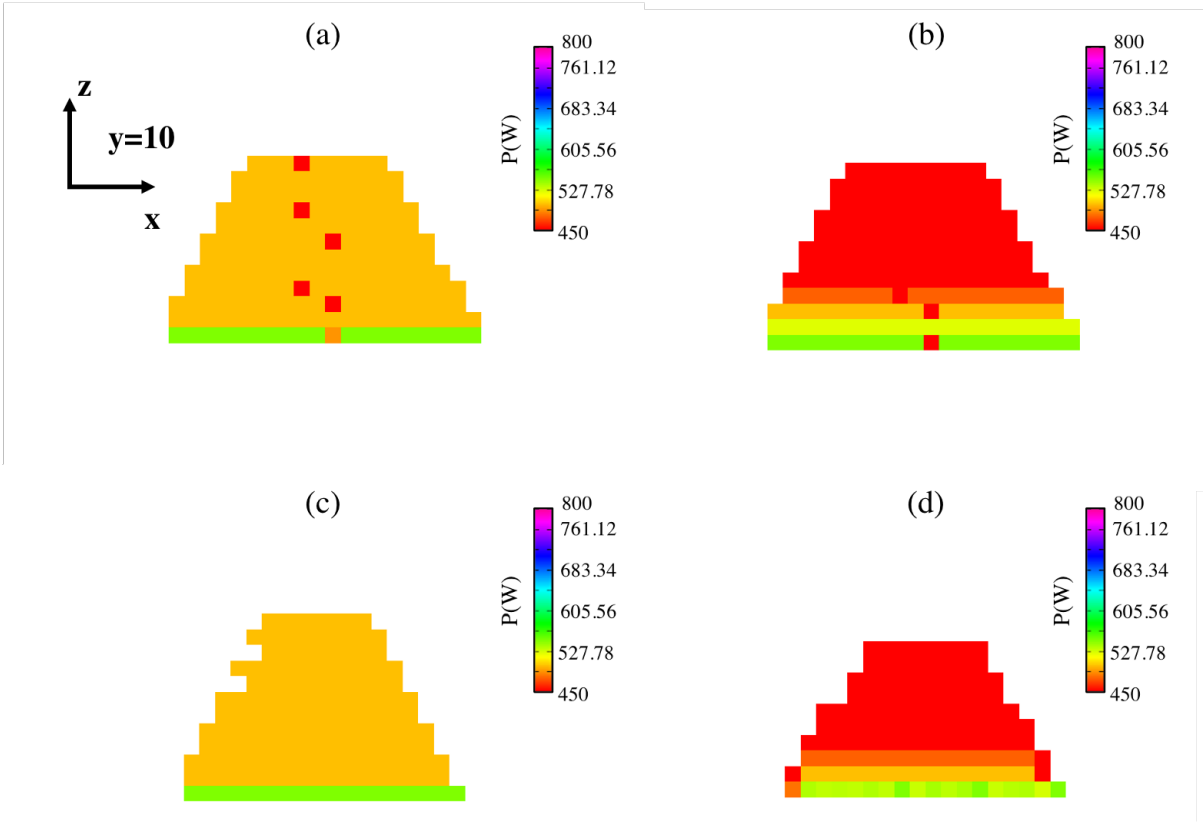

Source: Author

likely to be related to a minor local delivery of energy, as suggested in the DTMaps3D for each correspondent sample.

Although the pyramid mould configures another geometry, the analysis of the DTMap3D for those samples are well aligned to the one presented for the pyramids in this section. The reason for this is that both geometries are affected by the stair-case effect in the build of its angled faces, which together with the feed variation will potentially influence the part's rough finishing, as well as its bead height at those points with reduced feed speed. The regions with higher melt pool spot area will indicate a potential range with printing out of focus; and sudden reduction in laser power can indicate areas with lack of fusion and porosity related formation. For further information on the monitoring parameters, see all correspondent DTMap3D plots to the pyramids and pyramid moulds in Appendix A and Appendix B, respectively.

Figure 62 – DTMap3D plot of laser power from the pyramids sets built by contour at (a) 700 W and (b) gradient, and by zigzag at (c) 700 W and (d) gradient, at the xz-plane for Y=10.

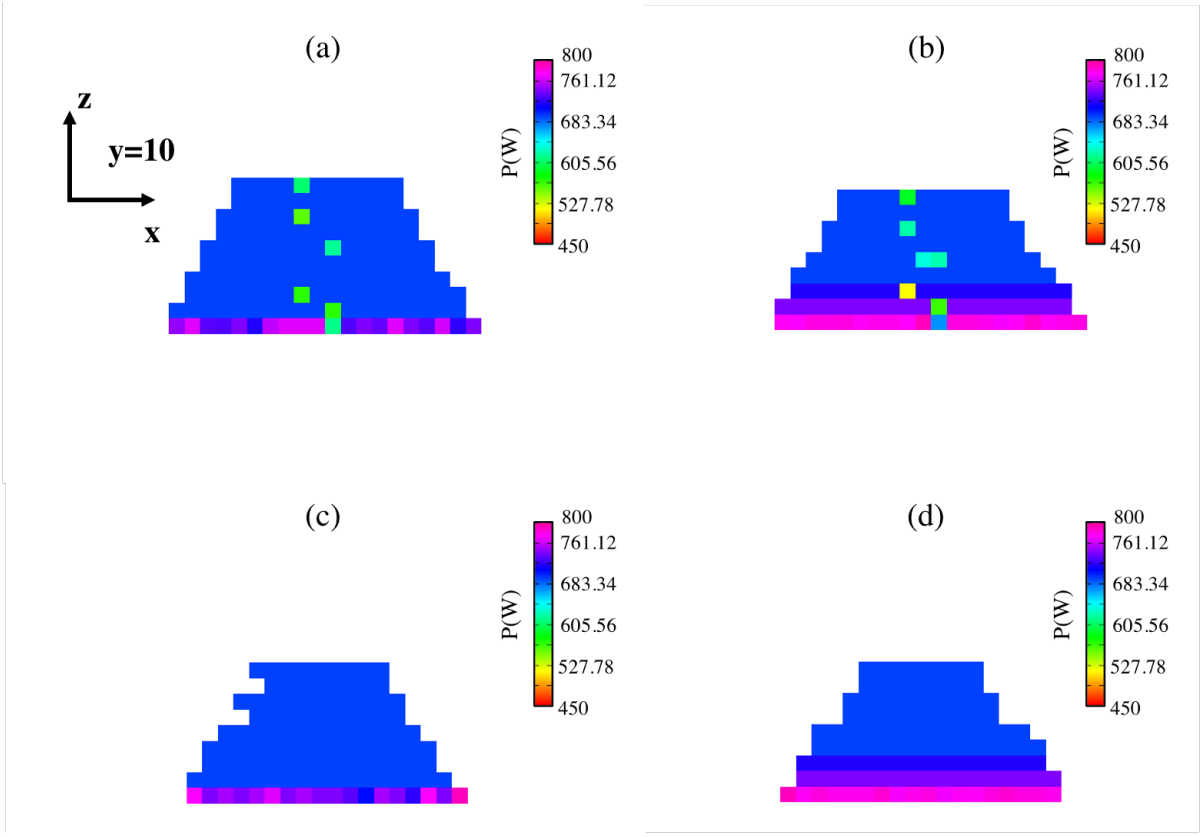

Source: Author

6 CONCLUSIONS

In this study, a novel methodology for collecting and visualizing data including laser power, feed speed, and melt pool area in DED operations was developed. The main conclusions that can be drawn from the results presented in this thesis are:

- The methodology for monitoring DED operations developed in this study was aided by the concept, design, and implementation of five software applications: DTConnect, MPIG, MPIP, DTMap2D, and DTMap3D. Each of these software applications plays an important role in monitoring data from the process, from data acquisition and processing to the graphic representation of the data.

- The DTMap inputs are files containing MPM and spatial data, acquired from the CNC by the newly developed DTConnect and MPIG applications and processed by MPIP. These tools have been demonstrated through a proof-of-concept case in which four geometry types (zigzag, thin wall, pyramid, and pyramid mold) were deposited.

- The maximum average data acquisition rate obtained through the current FANUC hardware by DTConnect was 10.03 ± 0.3 *pps*. Although the data can potentially be acquired at higher rates through optical system based hardware, the data sending rate from the CNC is still limited due to the amount of processing occurring in parallel by the FOCAS calls. For that reason, the rate of data acquisition and the image acquisition had to be adjusted.

- Two sets were experimentally evaluated in the build of the pyramid and mould pyramid geometries: one considering laser power at 500 W (and gradient: 550 to 450 W), and the other one at 700 W (and gradient: 800 to 700 W). These sets have given different microstructure and material quality. Regardless the printing strategy, contour or zigzag, to the lower power set, defects due to lack of fusion between beads and subsequent layers, as well as entrapped powder and pores were found in both geometries. With the increase in laser power, the energy delivered at the melt pool has increased in 40 %, being enough to significantly enhance the quality and homogeneity in both geometries, highly mitigating the defects aforementioned.

- The pyramid built with vertical gradient $550-450$ W in zigzag strategy has presented the higher percentage of porosity, estimated in 2.76%, whilst the set with 500 W produced the lowest (1.36%) from this set with 500 W.

- The percentage of porosity has decreased considerably (at least 5 times) with the increase of laser power to 700 W and its gradient. To the 700 W laser power set of

pyramids, it has also been observed an increase in porosity of, approximately, 60% when performing printing with laser power gradient.

- The sets with higher presence of lack of fusion were the ones built by contour and zigzag strategy with gradient laser power (550 to 450 W), whilst a decrease in this defect has been achieved with the increase in laser power.

- In the case of pyramid mould builds, defects such as lack of fusion, bad dilution, and porosity were observed in the sets with 500 W and gradient. However, it was reassured that the scanning strategy used affects the re-heating cycles of the part and, consequently, material solidification and the presence of defects. Scanning strategies that require long distances between deposition tracks, such as contour strategy, result in more defects such as pores and lack of fusion compared to those that minimize the time between tracks, such as the zigzag strategy.

- The study found that porosity levels decreased by about 63.2 % in pyramid mold parts built with constant laser power and 62.7 % in parts with a laser power gradient. There was no significant difference in porosity between sets built with the same scanning strategy but different laser power configuration. The reduction in defects due to porosity, lack of fusion, and bad dilution is dependent on the energy delivered to the melt pool, regardless of the geometry.

- A round top edge was found in the pyramid moulds produced by contour strategy, when compared to the final form of the parts produced in zigzag pathway. This difference was mainly noted in the sets produced at 700 W and gradient, which can be due to a loss of focus at the end of the build, adding up to the edged geometry, which is already know to have form deviation highly affect by deposition out of focus.

- The traditional thresholding method is not accurate for binarizing melt pool images, especially when the deposition occurs out of focus or at the borders. An adaptive thresholding method based on Otsu's method was proposed and applied to automatically categorize the threshold for each image during processing, forming the basis of the MPIP software. This new method can identify when the deposition has lost focus and has the potential to provide valuable data to correct z-increment during deposition. However, further investigation is required to explore this potential.

- From the DTMap3D plots, one could see that the feed speed is highly influenced by the scanning strategy, making zones with reduction in feed speed potential ones for presenting higher bead height, therefore form deviation defect by consequence.

- Higher levels of melt pool spot area were obtained in the sets with higher energy delivered; lower spot area took place in the first layers as a result of the heat

dissipation process to the substrate, whilst higher spot area was obtained most likely at the top and borders of the geometry.

- In DTMap3D, zones with a very high melt pool spot area can also represent regions in which the deposition had occurred out of focus. The reason for this regards the methodology for image processing developed in this research that allows zones of lose focus to stand out in melt pool spot area related data.

- In all sets, the laser power configuration tends to remain constant during deposition, except at points where it is starting or shutting off or when programmed to vary for each layer. Large-sized pores and lack of fusion were observed in the pyramids built using the contour strategy. Although further studies are needed to investigate the relationship between these defects and process parameters, the presence of high area pores and lack of fusion is likely to be related to a minor local delivery of energy, as suggested by the DTMap3D for each corresponding sample.

- The DTMap2D and DTMap3D were both able to display process variables in a color map and could potentially detect defect regions caused by deposition out of focus. This makes DTMap3D a potential tool for identifying critical regions for post-build inspection, and the software toolset is primarily used to accelerate the correlation between monitoring parameters and the quality of the as-built workpiece.

7 FUTURE WORK

The possibilities for future applications of this approach are vast. Although the demonstration described here focused on early-stage offline data processing for algorithm refinement, the ultimate goal of this research is to develop real-time data processing techniques for defect detection. Future work could include improving the sensitivity and accuracy of the DTMap3D by acquiring data at higher rates and conducting more in-depth studies of the presented melt pool image processing technique. Real-time generation of 3D plots and enabling feedback for layer z-increment, as well as increasing data sampling frequency, would add operational flexibility to this solution. Additionally, further evaluation of metallurgy correlated to spatial combinations of parameter and process signatures would increase confidence in the software pack presented here as a quantitative evaluation tool capable of identifying zones of defects with high levels of porosity, thermal cracks, lack of fusion, and other issues.

REFERENCES

AMINE, T.; NEWKIRK, J. W.; LIOU, F. An investigation of the effect of direct metal deposition parameters on the characteristics of the deposited layers. **Case Studies in Thermal Engineering**, v. 3, p. 21–34, 2014. ISSN 2214-157X. Available at: http://www.sciencedirect.com/science/article/pii/S2214157X14000070.

ARMSTRONG, M.; MEHRABI, H.; NAVEED, N. An overview of modern metal additive manufacturing technology. **Journal of Manufacturing Processes**, v. 84, p. 1001–1029, 2022. ISSN 1526-6125. Available at: https://www.sciencedirect.com/science/article/pii/S1526612522007459.

BI, G.; SUN, C.; GASSER, A. Study on influential factors for process monitoring and control in laser aided additive manufacturing. **Journal of Materials Processing Technology**, v. 213, n. 3, p. 463–468, 2013. ISSN 0924-0136. Available at: http://www.sciencedirect.com/science/article/pii/S0924013612003020.

BLAKEY-MILNER, B. *et al.* Metal additive manufacturing in aerospace: A review. **Materials & Design**, v. 209, p. 110008, 2021. ISSN 0264-1275. Available at: https://www.sciencedirect.com/science/article/pii/S0264127521005633.

BOHLEN, A. *et al.* Additive manufacturing of tool steel by laser metal deposition. **Procedia CIRP**, v. 74, p. 192–195, 2018. ISSN 2212-8271. 10th CIRP Conference on Photonic Technologies [LANE 2018]. Available at: http://www.sciencedirect.com/science/article/pii/S2212827118308783.

BURKHART, M.; AURICH, J. C. Framework to predict the environmental impact of additive manufacturing in the life cycle of a commercial vehicle. **Procedia CIRP**, v. 29, p. 408–413, 2015. ISSN 2212-8271. The 22nd CIRP Conference on Life Cycle Engineering. Available at: http://www.sciencedirect.com/science/article/pii/S2212827115005156.

COATES, P.; JONES, J. **Ambit - Additive Manufacturing Tools: System User Manual**. 1. ed. Leicestershire, United Kingdom, 2019. Product Designation:S7-325 and S7-2.

COELHO, R. T. *et al.* Mechanistic approach to predict real machining time for milling free-form geometries applying high feed rate. **Int J Adv Manuf Technol**, v. 46, p. 1103—-1111, 2010. Available at: https://link.springer.com/article/10.1007/s00170-009-2183-8#citeas.

DAS, T. *et al.* A comparative evaluation of the microstructural characteristics of l-ded and w-ded processed 316l stainless steel. **CIRP Journal of Manufacturing Science and Technology**, v. 40, p. 114–128, 2023. ISSN 1755-5817. Available at: https://www.sciencedirect.com/science/article/pii/S1755581722001894.

DEBROY, T. *et al.* Additive manufacturing of metallic components – process, structure and properties. **Progress in Materials Science**, v. 92, p. 112–224, 2018. ISSN 0079-6425. Available at: http://www.sciencedirect.com/science/article/pii/S0079642517301172.

DING, D. *et al.* Wire-feed additive manufacturing of metal components: technologies, developments and future interests. **The International Journal of Advanced**

Manufacturing Technology, v. 81, p. 465—481, 2015. Available at: https://link.springer.com/article/10.1007/s00170-015-7077-3#citeas.

DOUBENSKAIA, M. *et al.* Definition of brightness temperature and restoration of true temperature in laser cladding using infrared camera. **Surface and Coatings Technology**, v. 220, p. 244–247, 2013. ISSN 0257-8972. Proceedings of the fifth workshop RIPT (Les Rencontres Internationales sur la Projection Thermique). Available at: http://www.sciencedirect.com/science/article/pii/S0257897212010146.

EISENBARTH, D. *et al.* Spatial powder flow measurement and efficiency prediction for laser direct metal deposition. **Surface and Coatings Technology**, v. 362, p. 397–408, 2019. ISSN 0257-8972. Available at: http://www.sciencedirect.com/science/article/pii/S0257897219301446.

EVERTON, S. K. *et al.* Review of in-situ process monitoring and in-situ metrology for metal additive manufacturing. **Materials & Design**, v. 95, p. 431–445, 2016. ISSN 0264-1275. Available at: http://www.sciencedirect.com/science/article/pii/S0264127516300995.

F2792-12A, A. **ASTM F2792-12a: Standard Terminology for Additive Manufacturing Technologies**. 1st. ed. [*S.l.: s.n.*]: ASTM International, 2013. 1–3 p.

F3049-14, A. **ASTM F3049-14: Standard Guide for Characterizing Properties of Metal Powders Used for Additive Manufacturing Processes**. 1st. ed. [*S.l.: s.n.*]: ASTM International, 2014. 1–3 p.

F3187-16, A. **ASTM F3187-16: Standard Guide for Directed Energy Deposition of Metals**. 1st. ed. [*S.l.: s.n.*]: ASTM International, 2013. 1–22 p.

GAO, W. *et al.* The status, challenges, and future of additive manufacturing in engineering. **Computer-Aided Design**, v. 69, p. 65 – 89, 2015. ISSN 0010-4485. Available at: http://www.sciencedirect.com/science/article/pii/S0010448515000469.

GIBSON, B. T. *et al.* Melt pool size control through multiple closed-loop modalities in laser-wire directed energy deposition of ti-6al-4v. **Additive Manufacturing**, v. 32, p. 100993, 2020. ISSN 2214-8604. Available at: http://www.sciencedirect.com/science/article/pii/S2214860419317488.

GIBSON, I.; ROSEN, D.; STUCKER, B. **Additive Manufacturing Technologies: Rapid Prototyping to Direct Digital Manufacturing**. 2nd edition. ed. New York: Springer-Verlag, 2015. 498 p. ISBN 978 1 4939 2113 3.

GRIFFITH, M. L. *et al.* Understanding thermal behavior in the lens process. **Materials & Design**, v. 20, n. 2, p. 107–113, 1999. ISSN 0261-3069. Available at: http://www.sciencedirect.com/science/article/pii/S0261306999000163.

HART, J. **Additive Manufacturing: From 3D Printing to the Factory Floor**. 2020. Online course.

HE, W. *et al.* In-situ monitoring and deformation characterization by optical techniques; part i: Laser-aided direct metal deposition for additive manufacturing. **Optics and Lasers in Engineering**, v. 122, p. 74–88, 2019. ISSN 0143-8166. Available at: http://www.sciencedirect.com/science/article/pii/S0143816619304397.

HERZOG, D. *et al.* Additive manufacturing of metals. **Acta Materialia**, v. 117, p. 371–392, 2016. ISSN 1359-6454. Available at: http://www.sciencedirect.com/science/article/pii/S1359645416305158.

HSU, H.-W.; LO, Y.-L.; LEE, M.-H. Vision-based inspection system for cladding height measurement in direct energy deposition (ded). **Additive Manufacturing**, v. 27, p. 372–378, 2019. ISSN 2214-8604. Available at: https://www.sciencedirect.com/science/article/pii/S2214860418306572.

HU, D.; KOVACEVIC, R. Sensing, modeling and control for laser-based additive manufacturing. **International Journal of Machine Tools and Manufacture**, v. 43, n. 1, p. 51–60, 2003. ISSN 0890-6955. Available at: http://www.sciencedirect.com/science/article/pii/S0890695502001633.

HUA, T. *et al.* Research on molten pool temperature in the process of laser rapid forming. **Journal of Materials Processing Technology**, v. 198, n. 1, p. 454–462, 2008. ISSN 0924-0136. Available at: http://www.sciencedirect.com/science/article/pii/S0924013607007157.

KATTIRE, P. *et al.* Experimental characterization of laser cladding of cpm 9v on h13 tool steel for die repair applications. **Journal of Manufacturing Processes**, v. 20, p. 492—-499, 2015. ISSN 1526-6125. Available at: https://www.sciencedirect.com/science/article/abs/pii/S1526612515000638.

LAUWERS, B. *et al.* Hybrid processes in manufacturing. **CIRP Annals - Manufacturing Technology**, v. 63, p. 561–583, 12 2014.

LIANSUO, A. *et al.* Detection of pneumatic conveying by acoustic emissions. **Applied Sciences**, v. 9, p. 501, 02 2019.

LIOU, F. *et al.* Research and development of a hybrid rapid manufacturing process. **Proceedings of the Twelfth Annual Solid Freeform Fabrication Symposium**, p. 138–145, 01 2001. Available at: https://hdl.handle.net/2152/76157.

LIU, M. *et al.* A review of the anomalies in directed energy deposition (ded) processes & potential solutions - part quality & defects. **Procedia Manufacturing**, v. 53, p. 507–518, 2021. ISSN 2351-9789. 49th SME North American Manufacturing Research Conference (NAMRC 49, 2021). Available at: https://www.sciencedirect.com/science/article/pii/S2351978921001189.

LIU, S.; BRICE, C.; ZHANG, X. Interrelated process-geometry-microstructure relationships for wire-feed laser additive manufacturing. **Materials Today Communications**, v. 31, p. 103794, 2022. ISSN 2352-4928. Available at: https://www.sciencedirect.com/science/article/pii/S2352492822006523.

LORENZ, K. A. *et al.* A review of hybrid manufacturing. **26th Solid Freeform Fabrication Conference Proceedings**, p. 96–108, 2015.

MAHALE, R. S. *et al.* Processes and applications of metal additive manufacturing. **Materials Today: Proceedings**, v. 54, p. 228–233, 2022. ISSN 2214-7853. 5th International Conference on Advanced Research in Mechanical, Materials and Manufacturing Engineering-2021. Available at: https://www.sciencedirect.com/science/article/pii/S2214785321057436.

MISRA, S. *et al.* Investigation of ir pyrometer-captured thermal signatures and their role on microstructural evolution and properties of inconel 625 tracks in ded-based additive manufacturing. **Surface and Coatings Technology**, v. 447, p. 128818, 2022. ISSN 0257-8972. Available at: https://www.sciencedirect.com/science/article/pii/S0257897222007393.

MOTTA, M.; DEMIR, A. G.; PREVITALI, B. High-speed imaging and process characterization of coaxial laser metal wire deposition. **Additive Manufacturing**, v. 22, p. 497–507, 2018. ISSN 2214-8604. Available at: http://www.sciencedirect.com/science/article/pii/S221486041830085X".

MURUGAN, P. D. *et al.* A current state of metal additive manufacturing methods: A review. **Materials Today: Proceedings**, v. 59, p. 1277–1283, 2022. ISSN 2214-7853. International Conference Virtual Conference on Technological Advancements in Mechanical Engineering. Available at: https://www.sciencedirect.com/science/article/pii/S2214785321075258.

NUNEZ, H. H. L. **Desenvolvimento de técnicas de monitoramento para o processo de Directed Energy Deposition**. São Paulo: [*S.l.: s.n.*], 2021. 39 p. Relatório FAPESP.

NUNEZ, H. H. L. *et al.* Desenvolvimento de um programa de computador de baixo custo para integração de códigos g na fabricação e reparo de peças metálicas pelo processo de deposição por energia direcionada (ded). **28º SIICUSP**, 2020.

PURTONEN, T.; KALLIOSAARI, A.; SALMINEN, A. Monitoring and adaptive control of laser processes. **Physics Procedia**, v. 56, p. 1218–1231, 2014. ISSN 1875-3892. 8th International Conference on Laser Assisted Net Shape Engineering LANE 2014. Available at: http://www.sciencedirect.com/science/article/pii/S1875389214001837.

RIBEIRO, K. S.; MARIANI, F. E.; COELHO, R. T. A study of different deposition strategies in direct energy deposition (ded) processes. **Procedia Manufacturing**, v. 48, p. 663 – 670, 2020. ISSN 2351-9789. 48th SME North American Manufacturing Research Conference, NAMRC 48. Available at: http://www.sciencedirect.com/science/article/pii/S2351978920316103.

SAMPSON, R. *et al.* An improved methodology of melt pool monitoring of direct energy deposition processes. **Optics & Laser Technology**, v. 127, p. 106194, 2020. ISSN 0030-3992. Available at: http://www.sciencedirect.com/science/article/pii/S0030399219325149.

SREENIVASAN, R.; GOEL, A.; BOURELL, D. L. Sustainability issues in laser-based additive manufacturing. **Physics Procedia**, v. 5, p. 81—-90, 2010. ISSN 1875-3892. Available at: https://www.sciencedirect.com/science/article/pii/S187538921000550X.

SRIVASTAVA, M. *et al.* Wire arc additive manufacturing of metals: A review on processes, materials and their behaviour. **Materials Chemistry and Physics**, v. 294, p. 126988, 2023. ISSN 0254-0584. Available at: https://www.sciencedirect.com/science/article/pii/S0254058422012949.

STEEN, W.; MAZUMDER, J. **Laser material processing**. 4th edition. ed. [*S.l.: s.n.*]: Springer-Verlag, 2010. 558 p. ISBN 978-1-84996-061-8.

STRONG, D. *et al.* Hybrid manufacturing – integrating traditional manufacturers with additive manufacturing (am) supply chain. **Additive Manufacturing**, v. 21, p. 159–173,

2018. ISSN 2214-8604. Available at: http://www.sciencedirect.com/science/article/pii/S2214860417305444.

SUN, Z.; GUO, W.; LI, L. In-process measurement of melt pool cross-sectional geometry and grain orientation in a laser directed energy deposition additive manufacturing process. **Optics & Laser Technology**, v. 129, p. 106280, 2020. ISSN 0030-3992. Available at: http://www.sciencedirect.com/science/article/pii/S0030399219323989.

TAKUSHIMA, S. *et al.* Optical in-process height measurement system for process control of laser metal-wire deposition. **Precision Engineering**, v. 62, p. 23–29, 2020. ISSN 0141-6359. Available at: http://www.sciencedirect.com/science/article/pii/S0141635919307706.

TAN, Z. E. *et al.* Characterisation of porosity, density, and microstructure of directed energy deposited stainless steel aisi 316l. **Additive Manufacturing**, v. 25, p. 286–296, 2019. ISSN 2214-8604. Available at: http://www.sciencedirect.com/science/article/pii/S2214860417304037.

TANG, L.; LANDERS, R. G. Melt pool temperature control for laser metal deposition processes—part i: Online temperature control. **Journal of Manufacturing Science and Engineering**, v. 132, p. 011010, 2010.

TAPIA, G.; ELWANY, A. A review on process monitoring and control in metal-based additive manufacturing. **Journal of Manufacturing Science and Engineering**, v. 136, p. 1–10, 12 2014.

THOMPSON, S. M. *et al.* An overview of direct laser deposition for additive manufacturing; part i: Transport phenomena, modeling and diagnostics. **Additive Manufacturing**, v. 8, p. 36–62, 2015. ISSN 2214-8604. Available at: http://www.sciencedirect.com/science/article/pii/S2214860415000317.

TOYSERKANI, E.; KHAJEPOUR, A.; CORBIN, S. F. **Laser Cladding**. 1st edition. ed. Florida: CRC Press, 2005. 280 p. ISBN 978 0 8493 2172 6.

VANDONE, A.; VALENTE, A. Ai based monitoring system for ded part quality evaluation. **Procedia CIRP**, v. 107, p. 635–640, 2022. ISSN 2212-8271. Leading manufacturing systems transformation – Proceedings of the 55th CIRP Conference on Manufacturing Systems 2022. Available at: https://www.sciencedirect.com/science/article/pii/S2212827122003225.

WANG, M. L.; WANG, G. 9 - electromagnetic sensors for assessing and monitoring civil infrastructures. *In*: WANG, M. L.; LYNCH, J. P.; SOHN, H. (ed.). **Sensor Technologies for Civil Infrastructures**. Woodhead Publishing, 2014, (Woodhead Publishing Series in Electronic and Optical Materials, v. 55). p. 238–264. ISBN 978-0-85709-432-2. Available at: http://www.sciencedirect.com/science/article/pii/B9780857094322500097.

WENG, F. *et al.* A novel strategy to fabricate thin 316l stainless steel rods by continuous directed energy deposition in z direction. **Additive Manufacturing**, v. 27, p. 474–481, 2019. ISSN 2214-8604. Available at: http://www.sciencedirect.com/science/article/pii/S2214860418309175.

WHITING, J.; SPRINGER, A.; SCIAMMARELLA, F. Real-time acoustic emission monitoring of powder mass flow rate for directed energy deposition.

Additive Manufacturing, v. 23, p. 312–318, 2018. ISSN 2214-8604. Available at: http://www.sciencedirect.com/science/article/pii/S2214860417304128.

YAN, Z. *et al.* Review on thermal analysis in laser-based additive manufacturing. **Optics & Laser Technology**, v. 106, p. 427–441, 2018. ISSN 0030-3992. Available at: http://www.sciencedirect.com/science/article/pii/S0030399217317140.

YANG, Y. *et al.* Acoustic analysis of particle-wall interactions of plug flow in vertical pneumatic conveying. **Chemical Engineering Science**, v. 211, p. 115260, 2020. ISSN 0009-2509. Available at: http://www.sciencedirect.com/science/article/pii/S000925091930750X.

YU, J. *et al.* Mechanics and energy analysis on molten pool spreading during laser solid forming. **Applied Surface Science**, v. 256, n. 14, p. 4612–4620, 2010. ISSN 0169-4332. Available at: http://www.sciencedirect.com/science/article/pii/S0169433210002618.

YUAN, J. *et al.* A method for melt pool state monitoring in laser-based direct energy deposition based on densenet. **Measurement**, v. 195, p. 111146, 2022. ISSN 0263-2241. Available at: https://www.sciencedirect.com/science/article/pii/S0263224122004055.

ZENOU, M.; GRAINGER, L. 3 - additive manufacturing of metallic materials. *In*: ZHANG, J.; JUNG, Y. (ed.). **Additive Manufacturing**. Butterworth-Heinemann, 2018. p. 53–103. ISBN 978-0-12-812155-9. Available at: http://www.sciencedirect.com/science/article/pii/B9780128121559000037.

ZHAI, Y.; LADOS, D. A.; LAGOY, J. L. Additive manufacturing: Making imagination the major limitation. **JOM**, v. 66, p. 808–816, 2014. ISSN 1543-1851. Available at: https://link.springer.com/article/10.1007/s11837-014-0886-2#citeas.

ZHANG, G. *et al.* On-line size measurement of pneumatically conveyed particles through acoustic emission sensing. **Powder Technology**, v. 353, p. 195–201, 2019. ISSN 0032-5910. Available at: http://www.sciencedirect.com/science/article/pii/S0032591019303638.

ZHANG, Q.; YAO, J.; MAZUMDER, J. Laser direct metal deposition technology and microstructure and composition segregation of inconel 718 superalloy. **Journal of Iron and Steel Research, International**, v. 18, n. 4, p. 73–78, 2011. ISSN 1006-706X. Available at: http://www.sciencedirect.com/science/article/pii/S1006706X1160054X.

ZHANG, W. *et al.* Intergranular corrosion characteristics of high-efficiency wire laser additive manufactured inconel 625 alloys. **Corrosion Science**, v. 205, p. 110422, 2022. ISSN 0010-938X. Available at: https://www.sciencedirect.com/science/article/pii/S0010938X22003407.

ZHANG, Y. *et al.* 2 - additive manufacturing processes and equipment. *In*: ZHANG, J.; JUNG, Y.-G. (ed.). **Additive Manufacturing**. Butterworth-Heinemann, 2018. p. 39 – 51. ISBN 978-0-12-812155-9. Available at: http://www.sciencedirect.com/science/article/pii/B9780128121559000025.